https://doi.org/10.5194/egusphere-2026-6098
Preprint. Discussion started: 12 November 2026
© Author(s) 2026. CC BY 4.0 License.

Ice growth driven by the Wegener-Bergeron-Findeisen process in expansion chamber simulations: roles of ascent rate and particle sedimentation

Inyeob La[1], Wojciech W. Grabowski[2,3], Shin-ichiro Shima[1,4], and Seong Soo Yum[5,6]
[1]Graduate School of Information Science, University of Hyogo, Kobe, Japan
[2]MMM Laboratory, NSF National Center for Atmospheric Research, Boulder, CO, USA
[3]Institute of Geophysics, Faculty of Physics, University of Warsaw, Warsaw, Poland
[4]RIKEN Center for Computational Science, Kobe, Japan
[5]Climate and Environmental Research Institute, Korea Institute of Science and Technology, Seoul, Republic of Korea
[6]Department of Atmospheric Sciences, Yonsei University, Seoul, Republic of Korea

Correspondence to: Inyeob La (inyeob.la@gsis.u-hyogo.ac.jp) and Seong Soo Yum (ssyum@kist.re.kr)

Abstract. Mixed-phase clouds often glaciate through the Wegener–Bergeron–Findeisen process (WBF), in which ice crystals grow at the expense of supercooled droplets. In finite-volume laboratory chambers, however, WBF signatures can be obscured by sedimentation losses and limited residence time within the mixed-phase temperature range. We use a Lagrangian super-droplet configuration of the babyEULAG model to simulate an idealized 2 m-high expansion cloud chamber with condensation/immersion freezing and externally mixed soluble aerosol and dust ice-nucleating particles. We vary imposed ascent rate, soluble aerosol concentration, and gravity to examine how particle growth time and sedimentation affect WBF. WBF is evaluated using a normalized state-dependent ice-deposition diagnostic and paired EVAP and NOEVAP simulations that isolate the effect of droplet evaporation. From each pair, we calculate two response metrics: dQ_{ice}, the relative enhancement of domain-mean ice mixing ratio in EVAP compared with NOEVAP, and Δf_{ice}, the corresponding increase in ice mass fraction. With gravity, both metrics show a turnover with ascent rate under polluted, Seoul-like conditions: they increase from low to intermediate ascent rates as faster cooling reduces sedimentation losses, but decrease at higher ascent rates as mixed-phase residence time becomes too short for sustained depositional growth. Under lower soluble-aerosol concentrations, fewer, larger droplets sediment more efficiently, weakening the WBF response. Without gravity and particle loss, WBF decreases monotonically with ascent rate, indicating dominant residence-time control. These results highlight the importance of finite-depth particle losses when interpreting chamber-based WBF measurements.

1 Introduction

Mixed-phase clouds play a central role in the formation of precipitation and exert a strong influence on Earth's radiation budget and climate. In these clouds, ice crystals and supercooled liquid droplets can coexist at subfreezing temperatures, and the exchange of water vapor between the two phases strongly controls cloud lifetime, phase partitioning and

https://doi.org/10.5194/egusphere-2026-6098
Preprint. Discussion started: 12 November 2026
© Author(s) 2026. CC BY 4.0 License.

radiative properties (e.g. Korolev et al., 2017; Henneberg et al., 2017). In the classical picture, the Wegener–Bergeron–Findeisen process (WBF) describes how ice crystals grow by vapor deposition at the expense of surrounding supercooled droplets when the ambient vapor pressure lies between saturation over ice and saturation over liquid water (Wegener, 1911; Bergeron, 1935; Findeisen, 1938). This process efficiently converts supercooled liquid water into precipitation-sized ice particles and is widely regarded as one of the main microphysical pathways for precipitation formation and the evolution of mixed-phase clouds (Korolev et al., 2017).

Beyond its role in precipitation formation, the partitioning between supercooled liquid water and ice in mixed-phase clouds remains a long-standing challenge in weather and climate models, particularly in high-latitude stratiform clouds. Persistent Arctic mixed-phase clouds show that supercooled liquid can be maintained for long periods despite the presence of ice, even though mixed-phase cloud is microphysically unstable because ice can grow at the expense of liquid through the WBF process (e.g. Morrison et al., 2012). Similar issues arise over the Southern Ocean, where model differences in liquid-ice partitioning strongly affect cloud optical depth feedbacks and contribute substantially to uncertainty in the liquid water path response to warming (McCoy et al., 2015).

Despite this broader importance, classical descriptions often treat the WBF as operating whenever ice crystals and supercooled droplets coexist at subfreezing temperatures. In many conceptual and modeling studies, WBF is implicitly assumed to act in any mixed-phase cloud, independent of the detailed thermodynamic conditions. However, theoretical studies have shown that phase transformations in mixed-phase clouds can be organized into distinct regimes controlled by the thermodynamic forcing (supersaturation and ascent rate) and the integrated ice crystal surface area acting as a vapor sink (Korolev and Mazin, 2003; Korolev, 2007; Korolev and Field, 2008). In this framework, a threshold ascent rate delineates conditions under which ice growth occurs at the expense of evaporating liquid (the strict WBF regime) from conditions in which both phases can grow simultaneously or evaporate together. As a result, classical WBF is expected only within a limited range of environmental and microphysical conditions. More recent analytical work has extended this regime classification and emphasized how the thickness of the mixed-phase layer and the efficiency of WBF depend sensitively on ascent rate, ice concentration and temperature (Pinsky et al., 2015).

The importance of WBF has motivated a broad spectrum of modeling studies, ranging from theoretical and parcel-model analyses to cloud-resolving simulations and global climate models. Theoretical and process-level studies have shown that WBF does not occur automatically in all mixed-phase clouds, but is limited to thermodynamic and microphysical regimes controlled by ascent rate, vapor supersaturation, and the ice particle population (Korolev, 2007; Fan et al., 2011; Korolev et al., 2017). These process-level insights are important for large-scale models, because GCMs must parameterize the depletion of supercooled liquid water by ice growth and its sensitivity to aerosols and ice-nucleating particles. Global modeling studies have shown that changes in mixed-phase microphysics, including the treatment of the WBF and heterogeneous ice nucleation, can affect aerosol indirect effects and top-of-atmosphere radiation by several tenths of a watt per square meter (Lohmann and Hoose, 2009; Storelvmo et al., 2008, 2011).

https://doi.org/10.5194/egusphere-2026-6098
Preprint. Discussion started: 12 November 2026
© Author(s) 2026. CC BY 4.0 License.

At the cloud scale, LES combined with detailed observations has been used to evaluate WBF in natural mixed-phase clouds. For orographic mixed-phase clouds over complex Alpine terrain, Henneberg et al. (2017) showed that the interplay of lifting, advection, aerosol loading, and mixed-phase microphysics strongly affects the persistence of supercooled liquid water and the partitioning between liquid and ice, with WBF acting together with riming and aggregation to control precipitation efficiency. Related case studies over the Alps indicate that changes in flow direction relative to the mountain range, which modify the effective slope and ascent-rate history of air parcels, can shift clouds between long-lived mixed-phase states and rapidly glaciated states (Lohmann et al., 2016; Henneberg et al., 2017). More recently, within the CLOUDLAB project, glaciogenic cloud-seeding experiments in persistent wintertime stratiform clouds over Switzerland have been used to observe WBF-driven glaciation at high temporal and spatial resolution. Omanovic et al. (2024) compared these seeding signals with ICON simulations in large-eddy model using a two-moment bulk microphysics scheme. The model reproduced observed ice crystal number concentrations in many cases, but underestimated the rapid depletion of cloud droplets observed in the field, suggesting that the effective WBF conversion from liquid to ice was too slow under some conditions. This result highlights that the representation of mixed-phase microphysics, including depositional ice growth, droplet evaporation, hydrometeor size distributions, and sedimentation, can strongly affect the simulated WBF efficiency. These studies show that WBF in natural mixed-phase clouds is difficult to interpret because thermodynamic forcing, aerosol and INP populations, sedimentation, and other ice-growth pathways are tightly coupled. They also suggest that the simulated depletion of supercooled droplets can depend sensitively on how mixed-phase microphysics is represented. This does not imply that a Lagrangian particle-based model is required in all cases, but it motivates a controlled framework in which particle size, composition, evaporation, freezing, depositional growth, and sedimentation can be tracked more directly. For this reason, we use an idealized expansion-chamber configuration coupled to a Lagrangian super-droplet microphysics scheme to isolate how ascent rate, aerosol loading, and sedimentation control WBF signatures.

Two related challenges emerge from this body of work and motivate the present study. First, in natural clouds, it is difficult to isolate the WBF from other pathways such as riming, aggregation, homogeneous freezing and turbulent mixing, because the thermodynamic forcing and aerosol populations cannot be prescribed and because sedimentation continuously redistributes hydrometeors in space and time (Korolev et al., 2003, 2017; Pinsky et al., 2015). Second, numerical models are sensitive to poorly constrained assumptions about INP concentrations, aerosol composition and mixing state, and subgrid variability in ascent rate and relative humidity. All of these factors complicate efforts to evaluate WBF efficiency directly against observations and to translate theoretical thresholds into robust parameterizations. As a result, there is still no simple, experimentally grounded framework that links dynamical forcing, aerosol conditions, sedimentation and observable WBF signatures in a way that can be used both to design controlled chamber experiments and to interpret mixed-phase cloud behavior in the atmosphere. Developing such a framework for a finite expansion chamber and relating it to mixed-phase cloud conditions is the main objective of this study.

Laboratory cloud chambers provide a controlled framework for investigating cloud microphysical processes because thermodynamic trajectories and aerosol conditions can be prescribed in a well-defined environment. Recent laboratory studies

https://doi.org/10.5194/egusphere-2026-6098
Preprint. Discussion started: 12 November 2026
© Author(s) 2026. CC BY 4.0 License.

also show that mixed-phase cloud evolution in cloud chambers depends strongly on spatial heterogeneity, wall forcing, and particle removal (e.g., Yang et al., 2025). In a recent model intercomparison for the Pi Chamber, full-chamber simulations generally retained liquid droplets near the lower boundary, whereas simulations assuming a well-mixed domain, excluding the near-wall region, or using coarse grid spacing did not (Wang et al., 2026). In an expansion cloud chamber, pressure and temperature can decrease along a chosen trajectory that is dynamically equivalent to an imposed ascent rate, while the soluble aerosol population that acts as cloud condensation nuclei (CCN) and the INP population are specified a priori. This makes expansion chambers, in principle, ideal tools to isolate and quantify WBF, since the cooling rate, aerosol size distributions and INP spectra can be varied systematically. In practice, however, the finite height of the chamber and gravitational settling of hydrometeors impose strong constraints on how long supercooled liquid, ice crystals and their interaction can be maintained. Sedimentation can remove droplets and ice crystals from the sampled volume on time scales comparable to, or shorter than, the imposed cooling time. This may prevent WBF from fully developing in the chamber, even if the local thermodynamic conditions are favorable in an atmospheric cloud. Systematic studies on how such finite depth and particle sedimentation modify the WBF regimes predicted by the theory are still lacking.

In this study, we investigate how ascent rate, soluble aerosol loading, and sedimentation together control WBF-driven ice growth in an expansion cloud chamber. The simulated chamber geometry follows the 1.5 m × 1.5 m × 2 m design of the chamber currently under construction at the Korea Institute of Science and Technology (KIST). The physical chamber is intended to support both expansion and convection experiments, but here we focus on its expansion mode. Numerical simulations in this study are performed with the babyEULAG model, a three-dimensional nonhydrostatic anelastic Eulerian–semi Lagrangian model coupled to a Lagrangian super droplet microphysics scheme (Grabowski, 2020; Grabowski et al., 2019, 2024). For the present work, the standard babyEULAG configuration coupled with the Super-Droplet Method (SDM; Shima et al., 2009) is extended by implementing the condensation/immersion freezing scheme following Shima et al. (2020), and by imposing spatially uniform cooling and pressure tendencies that mimic effective ascent rates from 1 to 30 m s^{-1} in expansion mode. Collision–coalescence and other collection processes are not represented in the simulations. To characterize conditions relevant to WBF, we evaluate the thermodynamic saturation state together with a normalized state-dependent ice-deposition diagnostic based on the source–sink framework of Korolev (2007), and track the evolution of liquid water content, ice mass, ice fraction and crystal habits while systematically varying ascent rate, soluble aerosol concentration and INP loading. By comparing simulations with and without gravitational settling, as well as companion experiments in which liquid droplet evaporation is artificially suppressed, we separate the roles of cooling, WBF and particle sedimentation in controlling ice growth under conditions representative of the planned KIST cloud chamber.

2 Model setup

Numerical simulations in this study were performed with the babyEULAG model, a three-dimensional non-hydrostatic anelastic Eulerian model coupled to Lagrangian particle-based microphysics (i.e., using super-droplets; Shima et

https://doi.org/10.5194/egusphere-2026-6098
Preprint. Discussion started: 12 November 2026
© Author(s) 2026. CC BY 4.0 License.

al., 2009, 2020; Grabowski et al., 2019). In this framework, an ensemble of physical particles is represented by computational super-particles that carry particle attributes such as phase, radius, composition, and ice-particle morphology, together with multiplicity, which allows an explicit representation of droplet and ice particle size distributions and microphysical process rates at the particle level without prescribing fixed bulk relationships. The dynamical core is a simplified version of the EULAG model (http://www.mmm.ucar.edu/eulag), adapted for idealized chamber simulations and referred to as babyEULAG. Subgrid-scale turbulence is implicitly represented through the monotone multidimensional positive-definite advection transport algorithm (MPDATA), eliminating the need for explicit subgrid-scale parameterizations. Detailed descriptions of the dynamical core, numerical schemes, and the original chamber configurations can be found in Grabowski (2020) and Grabowski et al. (2024).

The computational domain is configured to approximate the expansion cloud chamber that is being constructed at the Korea Institute of Science and Technology (KIST). The physical chamber is cylindrical with an inner diameter of 1.5 m and a height of 2.0 m. In the model, this volume is represented by a rectangular domain with 38 × 38 × 101 grid points and uniform grid spacings of 0.04 m horizontally and 0.02 m vertically. Lateral boundaries of the computational domain are periodic, and the lower and upper boundaries are rigid lids with free-slip conditions for the horizontal velocity components. To mimic solid sidewalls within the horizontally periodic framework, internal wall regions are introduced at a prescribed grid point in each horizontal direction. Within three grid points of each internal wall plane, all three velocity components are relaxed toward zero, and the thermodynamic variables are nudged toward a prescribed wall state with a relaxation time scale of 0.1 s. Any super-droplet that is transported into a zone of 0.1 of horizontal or vertical grid length is removed from the domain. This represents particle wall loss processes and includes gravitational settling to the bottom plate.

For the present study, the babyEULAG configuration was modified from the convection-chamber setup used by Grabowski (2020), Grabowski et al. (2024) and La et al. (2026) to emulate an idealized expansion cloud chamber. Instead of maintaining a fixed vertical temperature gradient and constant pressure, the chamber is initialized with a horizontally and vertically uniform base-state temperature and pressure, with small random temperature perturbations of 0.1 K added to initiate fluctuations. A time-dependent, spatially uniform cooling and pressure decrease is then imposed to mimic an air parcel ascending at a prescribed constant ascent rate w. At each time step, tendencies for temperature and pressure are applied to all grid cells so that temperature and pressure follow a pseudo-adiabatic ascent trajectory for a given w. The effective ascent rate is treated as an external control parameter and is varied between 1 and 30 m s^{-1} across the simulation suite. The imposed expansion-cooling tendency is $\mathrm{d}T/\mathrm{d}t_{exp} = -(g/c_p)w$, and pressure p is decreased according to $\mathrm{d}p/\mathrm{d}t = -\rho g w$, where g is the gravitational acceleration, c_p is the specific heat of dry air at constant pressure, w is the prescribed equivalent ascent rate, and ρ is the chamber-mean moist-air density calculated from the current thermodynamic state. The model volume is fixed, so the expansion is represented thermodynamically rather than by explicitly changing the chamber volume. As pressure decreases, air density also decreases. To account for the expansion-induced decrease in air density, super-droplet multiplicities are reduced consistently with the decreasing air density so that particle number concentration decreases with air density and particle number mixing ratio is conserved during the prescribed expansion. In this treatment, super-droplet multiplicities are

https://doi.org/10.5194/egusphere-2026-6098
Preprint. Discussion started: 12 November 2026
© Author(s) 2026. CC BY 4.0 License.

adjusted while the total number of super-droplets is conserved. Boundary values for temperature, pressure, and water vapor mixing ratio are reset at every time step to the current interior mean, which suppresses the net fluxes across the boundaries and maintains a homogeneous mean thermodynamic state while still allowing small-scale fluctuations to develop.

Relative humidity is controlled in an idealized way to focus on microphysical responses to the imposed cooling. At the side walls, top and bottom lids, relative humidity is constrained to be equal to the instantaneous chamber mean. For temperatures above 0 °C, the boundary relative humidity is not allowed to exceed saturation with respect to liquid water, and at subfreezing temperatures it is not allowed to exceed saturation with respect to ice. This treatment is intended to mimic laboratory cloud chambers whose walls are coated with water or ice and therefore maintain the adjacent air at saturation with respect to the appropriate phase, as in Karlsruhe Institute of Technology's Aerosol Interactions and Dynamics in the Atmosphere (AIDA) cloud simulation chamber (Möhler et al., 2006) and the MRI cloud chamber built at the Meteorological Research Institute of the Japan Meteorological Agency (Tajiri et al., 2013). These constraints ensure that the mean state follows a simple thermodynamic path in which supersaturation is generated by cooling and consumed by phase changes, and they prevent the system from drifting to unrealistically high near-wall supersaturation over the course of a simulation. All simulations start from a horizontally and vertically uniform initial state with a temperature of 278.15 K and a relative humidity of 80 %, and are then subjected to the prescribed cooling corresponding to the chosen ascent rate.

The original babyEULAG configuration does not include ice phase microphysics. For the present work, condensation/immersion freezing processes were implemented by porting the corresponding scheme from the SCALE Super-Droplet Method (SCALE-SDM; Shima et al., 2020) into babyEULAG SDM. The freezing scheme uses an ice nucleating active surface (INAS) formulation, in which the number of active sites on an ice nucleating particle (INP) depends on particle surface area and temperature through an empirical parameterization. For mineral dust INP, we adopt the INAS parameterization derived from AIDA expansion chamber experiments by Connolly et al. (2009). The active-site density is parameterized as

$$n_s(T) = \begin{cases} a_1(T + a_2)^2, & T < -a_2 \\ 0, & T \geq -a_2 \end{cases} \quad (1)$$

where a_1=6.723780×10^9 m^{-2} °C^{-2} and a_2=20.78 °C. Here, $n_s(T)$ is the number of ice-nucleating active sites per unit dust surface area, with units of m^{-2}, and T is temperature in °C. In this framework, the probability of condensation/immersion freezing for a given super-droplet in a given timestep depends on its dust surface area and the local temperature, consistent with the singular hypothesis of heterogeneous freezing.

Figure 1 summarizes the prescribed dry aerosol size distributions and corresponding critical activation properties used in the expansion chamber simulations. The aerosol population is represented as an external mixture of soluble ammonium sulfate and Asian dust (AD). The soluble aerosol population, based on ground-based observations at Yonsei University in Seoul (Park et al., 2023a, b), provides CCN-active particles and is discretized into 30 logarithmically spaced dry-radius bins, with a baseline total number concentration of 11,400 cm^{-3}. The dust population provides INPs and is also discretized into 30 logarithmically spaced dry-radius bins spanning 0.035–1.0 μm, following the AD distribution reported by Möhler et al. (2006). To obtain a clear WBF signal within the finite residence time of the 2 m high chamber, the total dust concentration is scaled

https://doi.org/10.5194/egusphere-2026-6098
Preprint. Discussion started: 12 November 2026
© Author(s) 2026. CC BY 4.0 License.

to 1,500 cm^{-3} while preserving the prescribed spectral shape. This dust/INP concentration is intentionally idealized and much higher than typical atmospheric values. It was chosen to generate sufficient primary ice within the finite residence time of the 2 m chamber, where sedimentation and wall losses can rapidly deplete condensate and weaken the WBF signal. In the present model, additional ice sources such as secondary ice production and fragmentation are not represented; instead, ice initiation is restricted to condensation/immersion freezing associated with activated dust-containing droplets. Similar high-dust-loading strategies have been used in small adiabatic-expansion chamber experiments to facilitate controlled mixed-phase cloud formation. For example, Tajiri et al. (2013) used Arizona Test Dust (ATD) concentration of about 1000 cm^{-3} in the MRI expansion chamber with a height of 1.8 m and interpreted immersion/condensation freezing as the dominant ice nucleation mechanism. Park et al. (2025) also injected ATD particles at 1000 cm^{-3} in their mixed-phase expansion chamber experiment.

Dust particles are less hygroscopic than ammonium sulfate and therefore activate less readily as CCN. To quantify this contrast and to obtain the dust activation curves shown in Fig. 1a, dust activation is treated using the Frenkel-Halsey-Hill (FHH) adsorption framework, in which the equilibrium supersaturation over an insoluble particle is computed as (Kumar et al., 2009; Kumar et al., 2011):

$$S_{eq} = \exp\left[\frac{4\sigma M_w}{RT\rho_w D_p} - A_{FHH}\left(\frac{D_p - D_{dry}}{2D_{H_2O}}\right)^{-B_{FHH}}\right] - 1, \quad (2)$$

where D_{dry} is the dry dust particle diameter, D_p is the wet particle diameter, D_{H_2O} is the diameter of a water molecule, taken as 2.75 Å, and A_{FHH} and B_{FHH} are FHH adsorption parameters inferred from activation measurements. In this study we use A_{FHH}=1.82 and B_{FHH}=1.13, consistent with the East Asian soil-dust sample from the south-eastern edge of the Taklamakan Desert reported by Kumar et al. (2011). For each dry dust radius, the critical supersaturation S_c is obtained from the maximum of the equilibrium supersaturation curve $S_{eq}(D_p)$, determined by solving $dS_{eq}/dD_p = 0$. The corresponding wet particle diameter is used to diagnose the critical radius. These values are then used to construct the dust activation curves shown in Fig. 1a. Ice formation is represented through condensation/immersion freezing using the INAS formulation, so that only dust-containing droplets are allowed to freeze heterogeneously. Thus, soluble aerosol primarily governs the formation and growth of liquid droplets, whereas dust particles provide the ice-nucleating surface area for condensation/immersion freezing. Unlike Wang et al. (2026), who injected small ice crystals directly, our model explicitly represents droplet activation on dust particles, subsequent condensation/immersion freezing, and the resulting ice growth. Our aim is therefore to isolate the microphysical role of WBF rather than to reproduce a realistic atmospheric INP abundance.

https://doi.org/10.5194/egusphere-2026-6098
Preprint. Discussion started: 12 November 2026
© Author(s) 2026. CC BY 4.0 License.

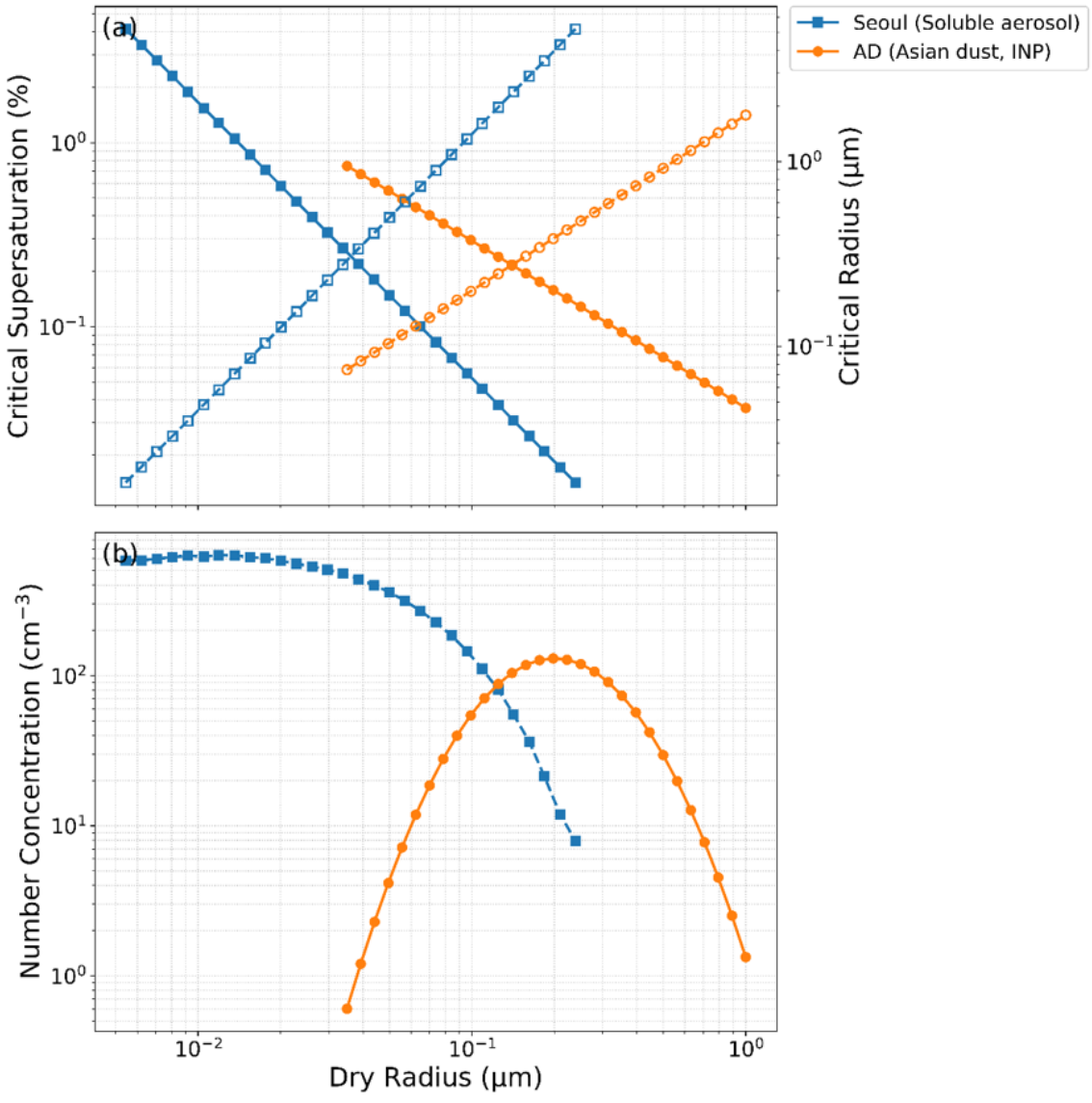


Figure 1. Critical activation properties and prescribed dry aerosol spectra used in the expansion chamber simulations. The panel (a) shows the critical supersaturation (left axis, filled markers) and critical radius (right axis, open markers) as functions of dry radius for the Seoul soluble aerosol (blue) and Asian dust (AD; orange); dust activation is computed using the FHH adsorption framework. The panel (b) shows the prescribed dry aerosol number size distributions for the same two aerosol types, each discretized into 30 dry-radius bins. These spectra are used to initialize externally mixed sulfate (CCN-active) and dust (INP) super-droplets in the model. The prescribed aerosol spectrum follows the dry-radius range used for the East Asian dust sample in the chamber-based parameterizations.

https://doi.org/10.5194/egusphere-2026-6098
Preprint. Discussion started: 12 November 2026
© Author(s) 2026. CC BY 4.0 License.

3 Results

3.1 Thermodynamic evolution and baseline expansion simulation

We first examine the thermodynamic evolution in the reference expansion simulations to verify that the prescribed expansion forcing described in Sect. 2 produces the intended parcel-like thermodynamic path. The reference case uses the Seoul soluble aerosol population, which acts as CCN, with a total number concentration of 11,400 cm^{-3}, the AD INP population scaled up to a total number concentration of about 1,500 cm^{-3}, and an effective ascent rate of w = 3 m s^{-1}. For comparison, another simulation is made with the ascent rate of w = 1 m s^{-1} but with all other conditions being the same. The model is then subjected to the prescribed cooling and pressure decrease that emulate a pseudo-adiabatic ascent at the chosen w. In the no-gravity simulation, gravity is disabled in both the dynamical and particle-motion calculations. Consequently, buoyancy-driven air motion and gravitational settling are absent. The air velocity remains zero, and super-droplets are not transported to the chamber boundaries. Thus, neither sedimentation loss nor wall loss occurs in this simulation, making it a parcel-like, loss-free reference.

Figure 2a compares the theoretical no-condensation adiabatic RH profile with the simulated domain-mean RH profiles, plotted against the equivalent ascent height $z = wt$. All simulations closely follow the theoretical curve. Their simulated LCLs are approximately 393 m, consistent with the theoretical value. This agreement confirms that the imposed cooling and pressure tendencies reproduce the intended thermodynamic trajectory. Figure 2b compares the domain-mean liquid-water mixing ratio, Q_{liq}, with the adiabatic liquid-water reference. The no-gravity simulation remains close to the adiabatic profile throughout the warm-cloud stage. This agreement shows that the prescribed expansion forcing and condensation treatment produce an approximately adiabatic liquid-water evolution when particle losses are absent. In contrast, the gravity-on simulations increasingly fall below the adiabatic reference after cloud formation. The departure is substantially larger for w = 1 m s^{-1} than for w = 3 m s^{-1}. To reach the same ascent height, the 1 m s^{-1} simulation requires three times as much physical time. Sedimentation and wall loss therefore act for a longer period, producing greater cumulative liquid-water depletion.

Figure 3 shows the corresponding time-height evolution of horizontally averaged Q_{liq} within the physical 2 m-high chamber for the gravity-on simulations with w = 1, 3, and 10 m s^{-1}, together with the no-gravity w = 3 m s^{-1} reference. In the no-gravity simulation, Q_{liq} remains nearly uniform with height because gravitational settling and particle removal at the chamber boundaries are absent. In contrast, the gravity-on simulations develop pronounced vertical inhomogeneity after cloud formation, reflecting the effects of particle sedimentation and wall loss. The magnitude of this depletion decreases systematically with increasing ascent rate. It is strongest for w = 1 m s^{-1}, weaker for w = 3 m s^{-1}, and substantially reduced for w = 10 m s^{-1}. Because the imposed expansion-cooling rate increases with the prescribed ascent rate, the higher-ascent-rate simulations reach a given chamber temperature in a shorter physical time. Over the approximately 1.8 km equivalent ascent interval shown in Fig. 3, the corresponding elapsed times are about 1800, 600, and 180 s for w = 1, 3, and 10 m s^{-1}, respectively. Thus, as the ascent rate increases, there is progressively less time for droplets to sediment and be removed at the chamber boundaries before the same thermodynamic state is reached. The reduced liquid-water depletion at w = 10 m s^{-1} therefore

https://doi.org/10.5194/egusphere-2026-6098
Preprint. Discussion started: 12 November 2026
© Author(s) 2026. CC BY 4.0 License.

demonstrates the decreasing cumulative influence of particle loss as the prescribed ascent rate increases and the cooling time shortens.

The temperature range shown in Figs. 2 and 3 is warmer than that required for appreciable ice formation under the INAS parameterization used here. The departures from the adiabatic reference therefore reflect liquid-droplet sedimentation and wall loss rather than ice growth or WBF. The detailed super-droplet removal pathways are shown in Fig. S1. These results establish the no-gravity simulation as a parcel-like reference and demonstrate how particle removal modifies liquid-water evolution in the finite chamber. They also provide the baseline for the mixed-phase WBF analysis in the following sections. Because direct observations from the planned KIST chamber are not yet available, we additionally compare the simulated particle size distributions with mixed-phase expansion experiments from the K-CPEC chamber (Park et al., 2025; Fig. S2). The chamber dimensions, INP type, and cooling pathway differ from those of the present setup, so this comparison is used only as a qualitative consistency check.

https://doi.org/10.5194/egusphere-2026-6098
Preprint. Discussion started: 12 November 2026
© Author(s) 2026. CC BY 4.0 License.

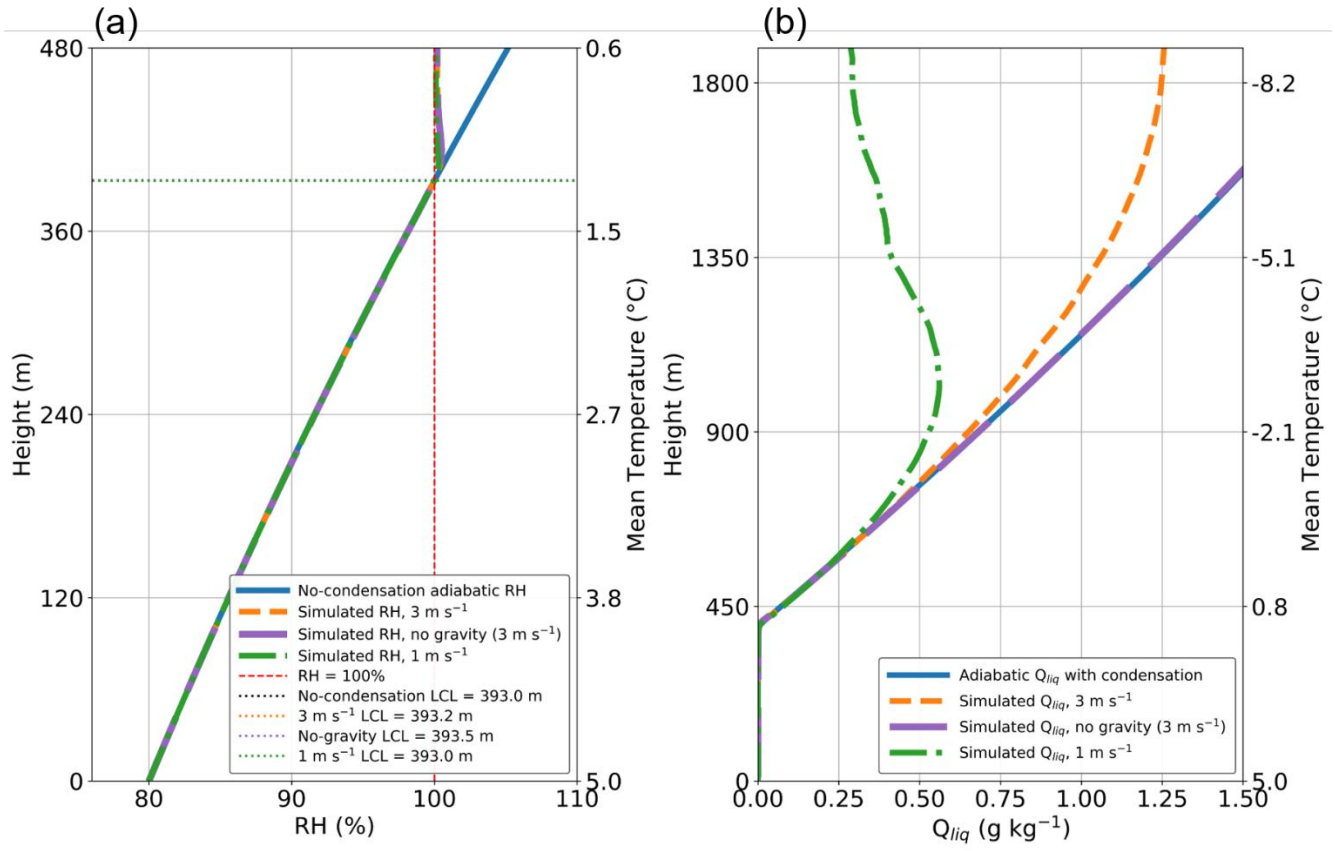


Figure 2. Thermodynamic evolution and domain-mean liquid water in the expansion simulations. Panels (a) and (b) show domain-averaged quantities plotted against the equivalent ascent height $z = wt$, which represents the prescribed pseudo-adiabatic ascent rather than the physical chamber height. The corresponding domain-mean chamber temperature is shown on the right axis. (a) Theoretical no-condensation adiabatic RH and simulated RH for the gravity-on w = 3 and 1 m s^{-1} cases and the no-gravity w = 3 m s^{-1} case. The RH = 100% line and the theoretical and simulated lifting condensation levels are marked. (b) Adiabatic liquid-water reference and simulated domain-mean Q_{liq} for the same three cases.

https://doi.org/10.5194/egusphere-2026-6098
Preprint. Discussion started: 12 November 2026
© Author(s) 2026. CC BY 4.0 License.

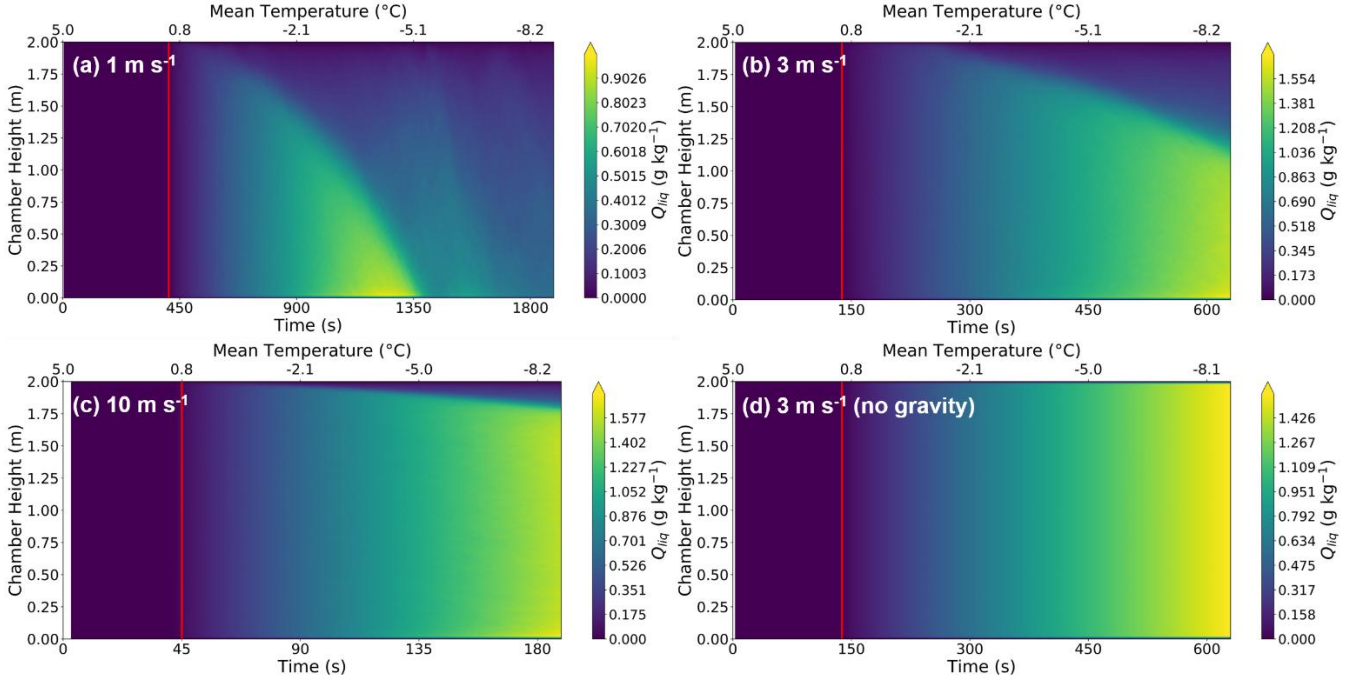


Figure 3. Time-height evolution of horizontally averaged liquid-water mixing ratio Q_{liq} within the physical 2 m-high chamber. Panels show (a) the gravity-on w = 1 m s^{-1} case, (b) the gravity-on w = 3 m s^{-1} case, (c) the gravity-on w = 10 m s^{-1} case, and (d) the no-gravity w = 3 m s^{-1} case. The upper axis indicates the domain-mean chamber temperature. The vertical red lines mark the onset of sustained cloud formation, defined as the first time when domain-averaged Q_{liq} exceeds 0.1 g kg^{-1}. Note that the time ranges on the horizontal axes are selected to give the same height change in all simulations, approximately 1.8 km.

3.2 Mixed-phase evolution and WBF signatures in the reference simulation

We next examine the mixed-phase evolution to identify WBF signatures. All simulations are initialized at 5 °C and 1000 hPa with a relative humidity of 80 %. The effective ascent rate is w = 3 m s^{-1}. We also include the corresponding no-gravity simulation and the slower gravity-on simulation with w = 1 m s^{-1}.

Figure 4 shows the time evolution of the domain-averaged liquid and ice particle size distributions. Panels (a,b) show the gravity-on w = 1 m s^{-1} case, panels (c,d) show the gravity-on w = 3 m s^{-1} case, panels (e,f) show the gravity-on w = 10 m s^{-1} case, and panels (g,h) show the no-gravity w = 3 m s^{-1} case. In all cases, a persistent submicron haze mode remains at wet diameters $D \lesssim 0.2$ μm. Particles larger than approximately 0.2 μm preferentially activate and form the cloud-droplet mode. In the gravity-on w = 3 m s^{-1} simulation, the liquid mode initially grows to diameters of approximately 20 μm. Ice crystals appear after the temperature decreases below -20 °C, consistent with the INAS parameterization in Eq. (1). The ice mode then broadens rapidly and reaches diameters of order 100 μm. At the same time, the liquid mode weakens and nearly disappears at approximately 23 min. Large droplets and ice crystals are continuously removed by sedimentation and wall loss. The no-

https://doi.org/10.5194/egusphere-2026-6098
Preprint. Discussion started: 12 November 2026
© Author(s) 2026. CC BY 4.0 License.

gravity simulation follows a different evolution. As shown in Fig. 4g, many droplets grow to diameters larger than 10 μm. As condensational growth depletes the supersaturation, droplets formed on the smaller aerosol particles, which require higher critical supersaturations, likely shrink toward the haze mode and deactivate. Thus, there is a clear separation of activated large droplets and unactivated and deactivated haze particles. After ice formation begins at approximately 20 min, the ice mode grows toward substantially larger diameters than in the gravity-on case. Because sedimentation and wall loss are absent, these large ice particles remain in the domain and continue to grow by vapor deposition. The resulting ice size distribution is therefore broader and shifted toward larger sizes than in the corresponding gravity-on simulation. For the gravity-on w = 1 m s^{-1} simulation, the transition from the liquid-dominated stage to the ice-dominated stage occurs later (note that x-axis scale is different for these two panels). Liquid droplets persist to lower temperatures, and the ice population develops more gradually. Without microphysical feedback, the slower cooling requires three times as much physical time to reach the same thermodynamic state as the w = 3 m s^{-1} case. With w = 10 m s^{-1} (Figs. 4e and 4f), the chamber reaches the same mixed-phase temperature range much more rapidly than with $w = 3$ m s^{-1}. Consequently, sedimentation and wall loss have less time to deplete the liquid-droplet population, and the liquid mode remains more distinct at lower temperatures. At the same time, the shorter physical growth period limits the time available for depositional ice growth, so the ice mode develops over a shorter interval and is less broadened toward large sizes than in the $w = 3$ m s^{-1}case. Sedimentation and wall loss therefore reduce the droplet and INP reservoirs before condensation/immersion freezing becomes efficient. This produces a smaller and less abundant ice population.

To further relate the simulated evolution to the prescribed INP spectrum and sedimentation loss, Fig. 5 shows the size-resolved origin of ice particles with diameter $D \geq 2$ µm. To construct Fig. 5, all ice super-particles with $D \geq 2$ µm were selected at each output time. Each selected ice particle was then classified according to the dry-size bin of the original INP from which it formed. The contribution of each INP size bin was calculated as the number fraction of ice super-particles in that bin relative to the total number of selected ice super-particles with $D \geq 2$ µm. Ice particles with $D \geq 2$ µm are preferentially associated with relatively large INPs, which tend to freeze earlier because the INAS freezing probability increases with particle surface area. However, the largest INP size bin does not necessarily dominate because its contribution also depends on the initial number of INPs in each bin and on the freezing temperatures randomly assigned from the INAS probability distribution. After the initial ice-formation period, the fractional contribution from INPs with dry radius of 0.088–0.111 µm generally increases with time (Fig. 5b), indicating that the smaller-radius INP range makes an increasingly important contribution to the $D \geq 2$ µm ice population as the simulation proceeds. The sharp increase near the end of the simulation, as the chamber temperature approaches −38 °C, occurs close to the homogeneous-freezing regime and should therefore be distinguished from the heterogeneous ice evolution discussed above.

https://doi.org/10.5194/egusphere-2026-6098
Preprint. Discussion started: 12 November 2026
© Author(s) 2026. CC BY 4.0 License.

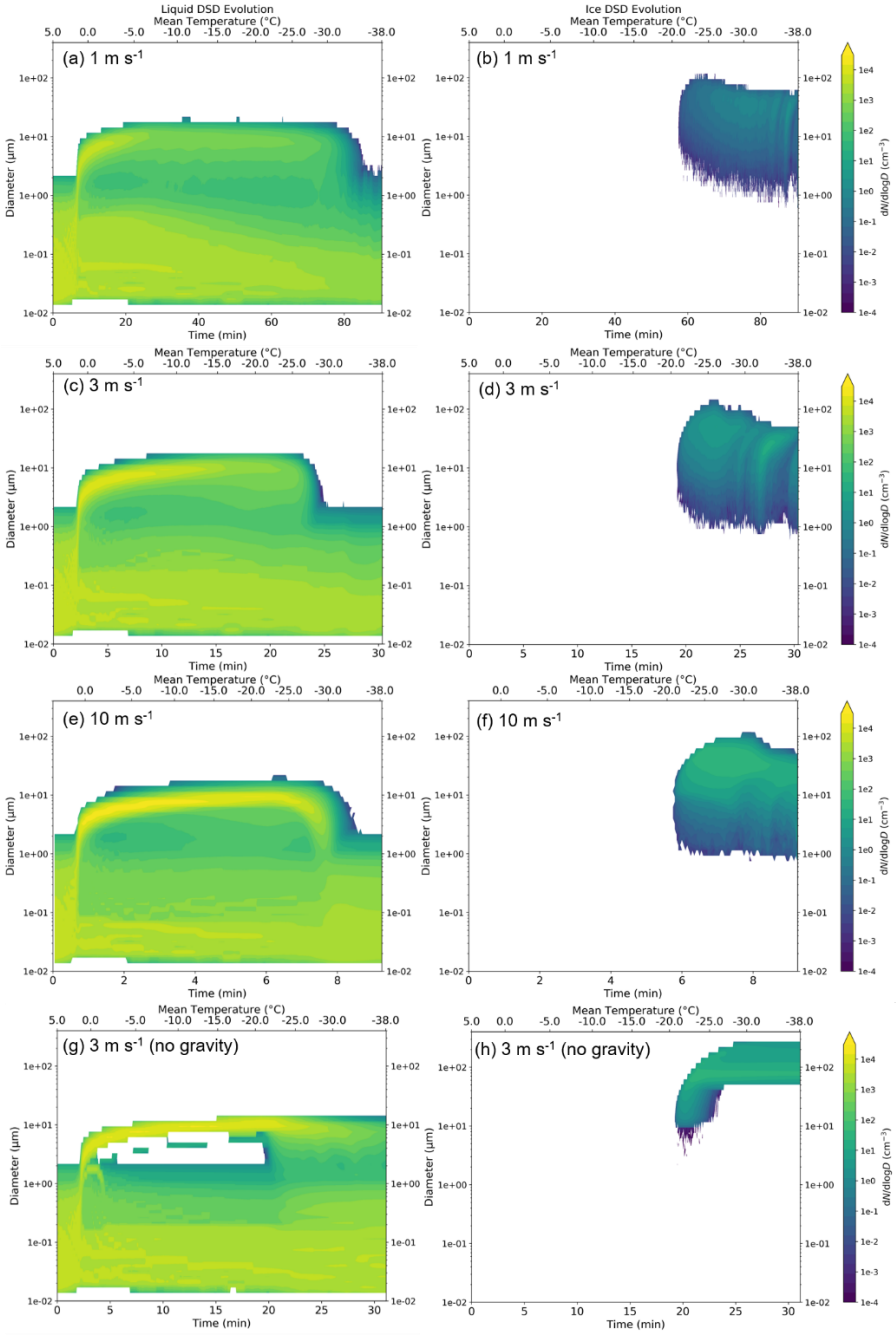


Figure 4. Time evolution of domain-averaged particle size distributions for the polluted EVAP mixed-phase expansion simulations. Panels (a,b) show the gravity-on w = 1 m s^{-1} case, panels (c,d) show the gravity-on w = 3 m s^{-1} case, panels (e,f) show the gravity-on w = 10 m s^{-1} case, and panels (g,h) show the no-gravity w = 3 m s^{-1} case. The left column shows liquid droplets, and the right column shows ice crystals. The upper axis indicates the domain-mean chamber temperature.

https://doi.org/10.5194/egusphere-2026-6098
Preprint. Discussion started: 12 November 2026
© Author(s) 2026. CC BY 4.0 License.

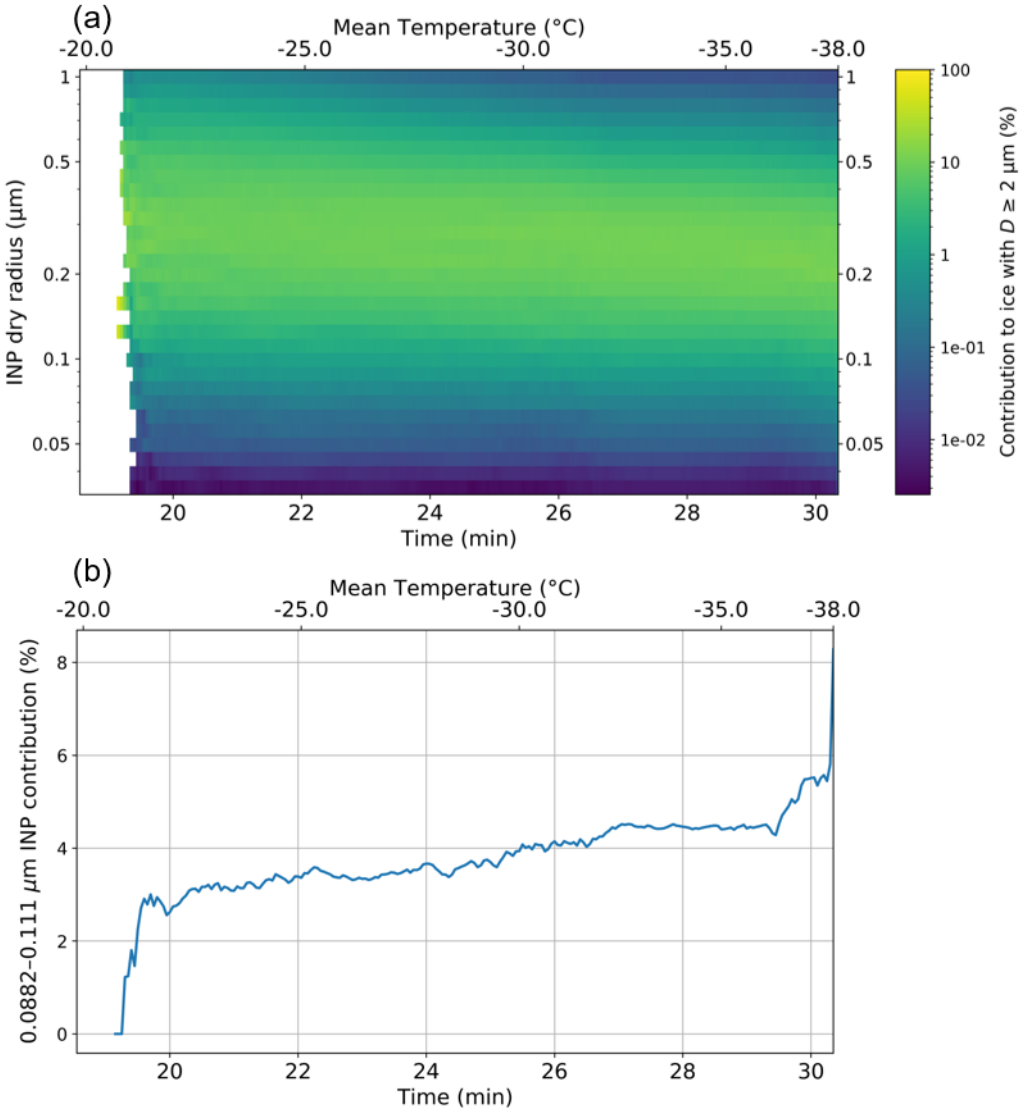


Figure 5. Origin contribution to ice with $D \geq 2$ µm by INP dry radius for the reference polluted case (Seoul aerosol) with an effective ascent rate of $w = 3$ m s^{-1}. (a) time evolution of the percent contribution from each INP dry-radius class to the population of ice with $D \geq 2$ µm, shown as a heatmap (top axis indicates mean temperature). (b) Time series of the fractional contribution from INPs with dry radius of 0.088–0.111 µm to the population of ice with $D \geq 2$ µm.

Korolev (2007) discusses the impact of the mean ascent on growth of water droplets and ice crystals carried by an adiabatic air parcel. The relevant parameter is the magnitude of the water vapor pressure e together with its relation to the saturated water vapor pressure over liquid water, e_{sw}, and the saturated water vapor pressure over ice, e_{si} (see Fig. 1 and eqs. 1-3 in Korolev 2007). For a given below-freezing temperature, e_{sw} is always larger than e_{si}. It follows that both water droplets

https://doi.org/10.5194/egusphere-2026-6098
Preprint. Discussion started: 12 November 2026
© Author(s) 2026. CC BY 4.0 License.

and ice particles grow when e is larger than e_{sw}, that is, when $e > e_{sw} > e_{si}$. When the water vapor pressure is between water and ice saturation, that is, when $e_{sw} > e > e_{si}$, ice crystals grow and water droplets evaporate. This is the textbook WBF regime in which the ice field grows at the expense of the liquid water field. Finally, when e is below e_{si}, both water droplets and ice crystals evaporate. Korolev (2007) introduces two threshold vertical velocity scales that define conditions separating the three regimes. The threshold velocity scales depend on microphysical parameters of water and ice particles, the concentration and mean radius, see Eqs. 4 and 5 in Korolev (2007). The vertical velocity corresponding to the water and ice evaporation is negative (see Eq. 5 therein) and thus irrelevant to the expansion cloud chamber experiments. The vertical velocity separating $e > e_{s,w} > e_{s,i}$ regime from $e_{s,w} > e > e_{s,i}$ regime (i.e., the upper bound of the WBF regime) is defined as (Eq. 4 in Korolev 2007):

$$U^*_{z,K} = \left(\frac{e_{s,w}}{e_{s,i}} - 1\right)\eta N_i \bar{r}_i, \tag{3}$$

where N_i is the ice crystal number concentration, $\bar{r}_i$ is the mean ice crystal radius, and η is a temperature- and pressure-dependent coefficient representing the ratio of the ice-depositional sink coefficient to the thermodynamic supersaturation-production coefficient. The ice-depositional sink coefficient incorporates the diffusional and thermal resistances governing ice growth (Korolev and Mazin, 2003; see their Eq. 22 and Appendix D). $U^*_{z,K}$ represents the ascent rate required to maintain saturation with respect to liquid water against the depositional vapor sink from growing ice particles.

Thermodynamic conditions in chamber experiments and corresponding model simulations are not constrained to remain saturated with respect to liquid water. The vapor pressure evolves continuously in response to expansion cooling and microphysical vapor exchange through droplet condensation or evaporation and ice deposition. Sedimentation and wall loss additionally modify the particle concentrations and thereby indirectly affect vapor source/sink. We therefore evaluate the bulk source/sink conditions using the simulated domain-mean supersaturation with respect to ice and define the modified vertical velocity scale U^*_z as:

$$U^*_z = \left(\frac{e}{e_{s,i}} - 1\right)\eta N_i \bar{r}_i, \tag{4}$$

where e is the vapor pressure in the chamber, instead of $e_{s,w}$ in (3). U^*_z is positive as long as $e > e_{s,i}$, and $U^*_z = U^*_{z,K}$ when $e = e_{s,w}$. Because it depends on both the ice microphysical parameters (N_i and $\bar{r}_i$) and the vapor pressure e, U^*_z reflects overall thermodynamic conditions in the chamber that are also affected by the growing or evaporating cloud droplets. Following the interpretation behind (3), U^*_z represents ascent rate required to maintain the vapor pressure e in the chamber, supersaturated with respect to ice and either supersaturated or subsaturated with respect of water. It follows that U^*_z can be used as a single parameter describing ice growth conditions in the chamber.

For convenience, the dimensionless parameter $u^*_z = U^*_z/w$ is introduced as a bulk source–sink diagnostic, where w is the prescribed effective ascent rate in the chamber experiment or simulation. In the absence of ice, $u^*_z = 0$. Once ice forms, u^*_z evolves in response to changes in the ice number–size term, $N_i\bar{r}_i$, and the simulated ice supersaturation. A value of $u^*_z < 1$ means that expansion-induced supersaturation production exceeds the instantaneous ice-depositional sink diagnosed at the simulated vapor pressure. Conversely, $u^*_z > 1$ means that the diagnosed ice-depositional sink exceeds the supersaturation source generated by the prescribed expansion rate, tending to lower the vapor pressure and thereby favour the onset or

https://doi.org/10.5194/egusphere-2026-6098
Preprint. Discussion started: 12 November 2026
© Author(s) 2026. CC BY 4.0 License.

maintenance of $S_{liq} < 0$. In the model simulations, u_z^* evolves continuously as the thermodynamic and microphysical conditions change inside the chamber. The WBF regime itself is diagnosed directly from the chamber thermodynamic state rather than from u_z^*. Specifically, thermodynamic conditions favorable for WBF are identified by $S_{liq} < 0$ and $S_{ice} > 0$, corresponding to a vapor pressure between saturation over ice and saturation over liquid water. The supersaturations are defined as $S_{liq} = 100(e/e_{s,w}-1)$ and $S_{ice} = 100(e/e_{s,i}-1)$. In the model simulations, droplet activation, growth or evaporation, and depositional growth of individual particles are calculated directly by the SDM microphysics. The time evolution of the domain-averaged normalized effective ascent-rate diagnostic, u_z^*, and the corresponding supersaturations is shown in Fig. 6. Panels (a,b) show the gravity-on w = 3 m s^{-1} simulation, panels (c,d) show the no-gravity w = 3 m s^{-1} simulation, and panels (e,f) show the gravity-on w = 1 m s^{-1} simulation.

In the gravity-on w = 3 m s^{-1} simulation, u_z^* is initially much smaller than unity because the ice-particle concentration and characteristic sizes are small. During this period, S_{liq} remains close to zero, and the supersaturation produced by expansion cooling is predominantly consumed by liquid-droplet condensation. After ice crystals form and grow, the ice number–size term increases and the diagnosed depositional sink strengthens. Consequently, u_z^* increases rapidly and exceeds unity at approximately 21 min. At nearly the same time, S_{liq} becomes negative while S_{ice} remains positive. This thermodynamic transition favors vapor deposition onto ice and evaporation of supercooled liquid droplets, consistent with the weakening of the liquid-droplet mode and growth of the ice mode shown in Figs. 4c and 4d. Before appreciable ice formation, above -20 °C, the spatial variability of both supersaturations remains small. Once stochastic freezing begins, grid-to-grid differences in the number and size of ice particles produce spatially heterogeneous depositional sinks. Consequently, the standard deviations of both S_{liq} and S_{ice} increase as the ice population develops. Oscillations during the final 10 minutes likely arise from the competition between ice growth and particle loss. Ice growth increases the ice number–size term but simultaneously consumes water vapor, reducing S_{ice} and limiting further deposition. Sedimentation and wall loss reduce the ice population, while continued expansion cooling restores ice supersaturation. Because u_z^* depends on both the ice number–size term and S_{ice}, these coupled changes modulate the diagnosed u_z^*.

The no-gravity w = 3 m s^{-1} simulation develops larger and smoothly evolving u_z^* than the corresponding gravity-on simulation. Because gravitational settling and wall loss are absent, ice particles generated by stochastic freezing remain near the locations where they formed and continue to grow. This enhances the contrast between ice-rich regions, where depositional growth strongly depletes water vapor, and ice-free regions, where the depositional sink remains weak. Moreover, because buoyancy-driven air motion is absent, these spatial differences in the ice population and vapor field are not efficiently redistributed by the flow. The combined effects of particle retention and weak dynamical mixing therefore allow the heterogeneous depositional sinks to persist and intensify, resulting in the substantially larger standard deviation of S_{ice} and the accompanying increase in the variability of S_{liq}. After reaching a maximum, u_z^* gradually decreases in the no-gravity simulation despite the persistence of large ice crystals in the chamber. Because Eq. (4) explicitly depends on the simulated S_{ice}, depositional growth consumes water vapor and reduces the ice supersaturation. The resulting weakening of the vapor-pressure driving force limits further ice growth and lowers the diagnosed u_z^*. Thus, although the ice population remains large, its

https://doi.org/10.5194/egusphere-2026-6098
Preprint. Discussion started: 12 November 2026
© Author(s) 2026. CC BY 4.0 License.

subsequent depositional growth becomes increasingly limited, consistent with the persistent large-particle ice mode shown in Figs. 4g and 4h.

In the gravity-on w = 1 m s^{-1} simulation, both the increase in u_z^* and the transition to negative S_{liq} are delayed. The slower expansion cooling requires three times as much physical time to reach the same thermodynamic state as in the w = 3 m s^{-1} simulations. Sedimentation and wall loss therefore act for a longer period before efficient freezing occurs, reducing the available droplet and INP populations. Consequently, fewer ice crystals are produced, the ice number–size term develops more gradually, and the diagnosed depositional sink remains weaker. The value of u_z^* remains below or near unity for a longer period, and S_{liq} becomes negative only at lower temperatures. This delayed evolution is consistent with the persistence of supercooled liquid droplets to lower temperatures (Figs. 4a and 4b). The oscillations in the final few minutes resemble those in the gravity-on 3 m s^{-1} simulation (Figs. 6a and 6b).

https://doi.org/10.5194/egusphere-2026-6098
Preprint. Discussion started: 12 November 2026
© Author(s) 2026. CC BY 4.0 License.

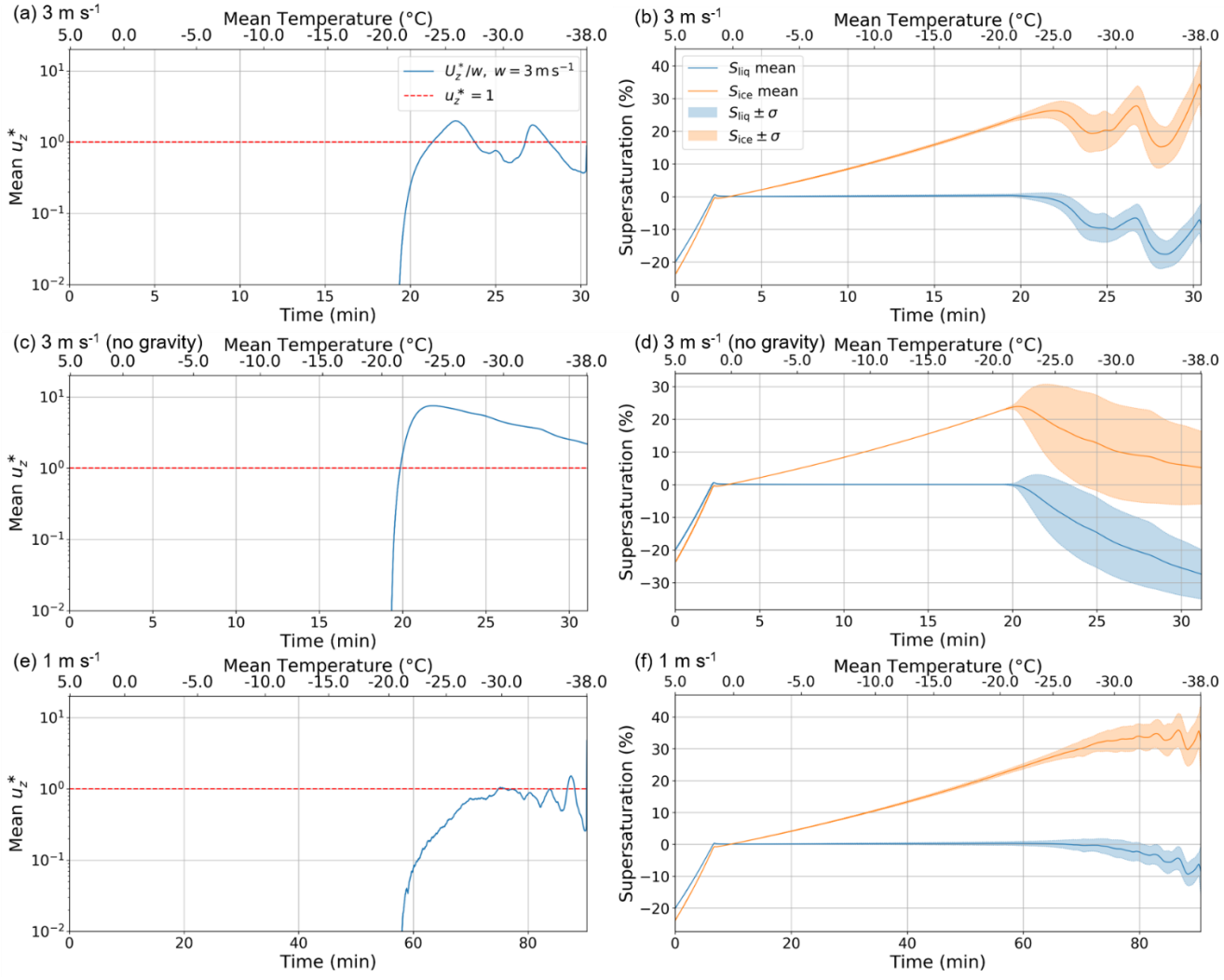


Figure 6. Normalized state-dependent ice-deposition diagnostic and supersaturation evolution for the polluted EVAP simulations. Panels (a,b) show the gravity-on w = 3 m s^{-1} case, panels (c,d) show the no-gravity w = 3 m s^{-1} case, and panels (e,f) show the gravity-on w = 1 m s^{-1} case. The left column shows the domain-mean normalized state-dependent ice-deposition diagnostic, $u_z^* = U_z^*/w$. The red dashed line marks $u_z^* = 1$, corresponding to equality between the diagnosed ice-depositional sink and the expansion-induced supersaturation source. The right column shows the corresponding domain-mean supersaturations with respect to liquid water, S_{liq}, and ice, S_{ice}. Shaded bands indicate $\pm 1\sigma$, where σ is the domain standard deviation. The upper axes indicate the domain-mean chamber temperature.

https://doi.org/10.5194/egusphere-2026-6098
Preprint. Discussion started: 12 November 2026
© Author(s) 2026. CC BY 4.0 License.

3.3 Role of liquid droplet evaporation

To isolate the contribution of the WBF to ice growth, we execute paired simulations for a range of ascent rates and aerosol loadings. For each combination of soluble aerosol concentration and ascent rate, we execute two simulations. In the EVAP simulation, both condensational growth and evaporation of liquid droplets are included. In the companion NOEVAP simulation, cloud droplets can grow by condensation when the air is supersaturated, but they are not allowed to evaporate, that is, their sizes are maintained even when the air becomes subsaturated. All other aspects of the dynamics and microphysics are kept identical between the paired simulations. The NOEVAP simulation is used as a diagnostic sensitivity test to isolate the role of droplet evaporation by suppressing the evaporative vapor supply from liquid droplets to ice particles; it is not intended as a realistic chamber configuration. Because liquid droplet evaporation is intentionally suppressed, the NOEVAP cases do not represent a physically legitimate WBF and are not used to diagnose WBF-driven droplet depletion directly. Therefore, u_z^* is retained only as a diagnostic of the strength of the ice depositional vapor sink relative to the cooling-induced vapor supply.

Figure 7 shows evolutions of the domain-averaged u_z^* as a function of the mean cloud chamber temperature in all simulations with gravity. Lines with different colors represent different ascent rates. Panels (a) and (b) show the polluted case. Panels (c) and (d) show the relatively clean case, in which the soluble aerosol number concentration (N_{sol}) is reduced by a factor of 10 compared with the Seoul control (i.e., polluted) case. Oscillations for weak ascent rates come from the particle sedimentation resulting in chamber vertical inhomogeneity as discussed previously. In the EVAP simulations (left column), u_z^* increases as the cloud glaciates and often exceeds 1 over a substantial part of the mixed-phase temperature range, especially at larger ascent rates and in the polluted case. Values of $u_z^* > 1$indicate that the diagnosed ice-depositional sink exceeds the expansion-induced supersaturation source, favoring the onset or maintenance of $S_{liq} < 0$. The thermodynamic state is identified as favorable for WBF when $S_{liq} < 0$ and $S_{ice} > 0$, as discussed previously. In the NOEVAP simulations (right column), the increase in u_z^* is much weaker and the curves remain below or close to unity for most cases. This occurs because suppressing droplet evaporation removes the crucial vapor source, limiting depositional growth of ice and keeping the ice-crystal surface area small. As a result, the depositional vapor sink by ice remains weak relative to the cooling-induced vapor supply, and u_z^* stays below or close to unity. The sharp changes near −38 °C in the NOEVAP simulations are associated with the same cold-end homogeneous freezing transition shown in Fig. 5.

To examine whether this diagnosed vapor-sink strength leads to liquid-water subsaturation, Figure 8 shows the domain-mean S_{liq}, as a function of mean chamber temperature for the same set of simulations. Unlike u_z^*, which diagnoses the strength of the ice depositional vapor sink, S_{liq} provides the direct thermodynamic indicator of whether liquid droplets tend to evaporate. In the polluted EVAP simulations, S_{liq} becomes negative over a broad mixed-phase temperature range, indicating the conditions favorable for WBF-driven droplet evaporation. The NOEVAP simulations show similar range of decrease but the trends differ depending on the ascent rate. In the clean simulations, S_{liq} remains positive longer, especially at the smallest ascent rates, consistent with weaker ice production, smaller total ice surface area, and reduced depositional vapor uptake. Together, Figures 7 and 8 show that efficient WBF-driven liquid depletion requires both a sufficiently strong ice depositional

https://doi.org/10.5194/egusphere-2026-6098
Preprint. Discussion started: 12 November 2026
© Author(s) 2026. CC BY 4.0 License.

sink and the availability of liquid droplets that can evaporate under liquid-subsaturated conditions. The corresponding supersaturation with respect to ice, S_{ice}, is shown in Fig. S5 and remains positive throughout most of the mixed-phase temperature range, confirming that the negative S_{liq} values occur while the air remains supersaturated with respect to ice.

https://doi.org/10.5194/egusphere-2026-6098
Preprint. Discussion started: 12 November 2026
© Author(s) 2026. CC BY 4.0 License.

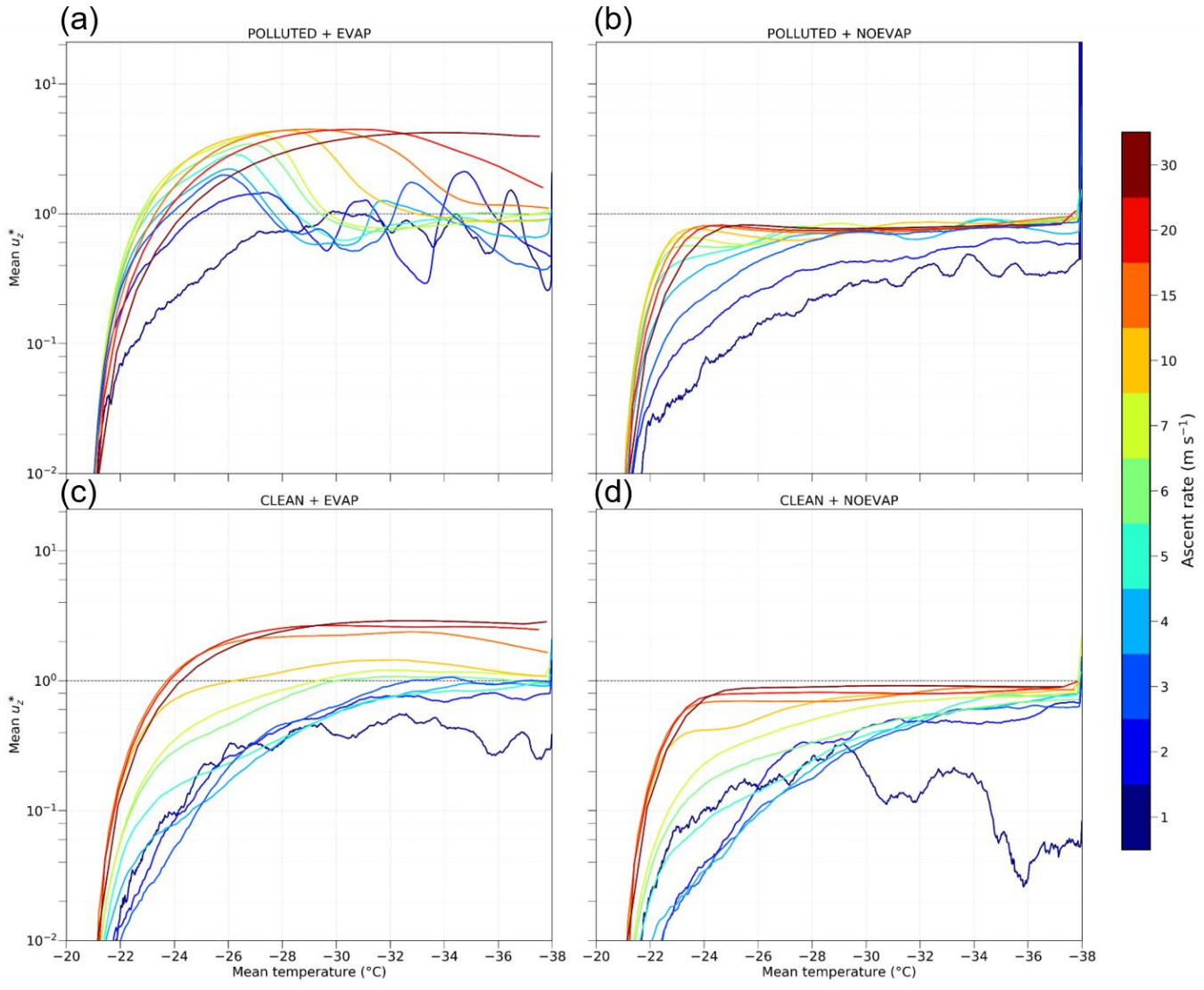


Figure 7. The domain-mean u_z^* as a function of mean cloud chamber temperature for all sensitivity simulations. The top row shows the polluted Seoul case and the bottom row shows the N_{sol}-reduced (clean) case. The left column corresponds to simulations with liquid droplet evaporation (EVAP) and the right column to simulations without evaporation (NOEVAP). Line color indicates the imposed ascent rate from 1 to 30 m s^{-1}. The vertical axis is shown on a logarithmic scale.

https://doi.org/10.5194/egusphere-2026-6098
Preprint. Discussion started: 12 November 2026
© Author(s) 2026. CC BY 4.0 License.

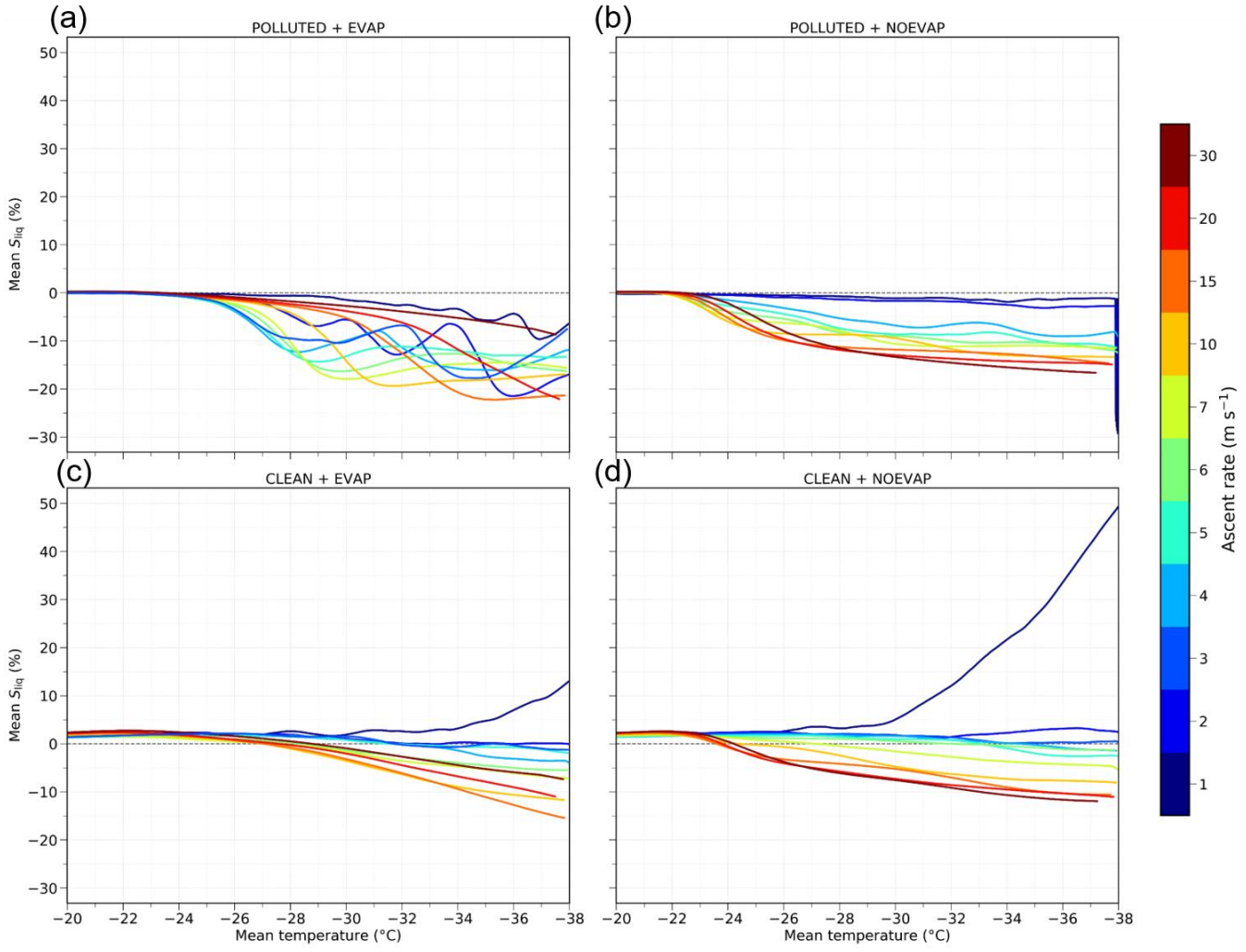


Figure 8. Same as Fig. 7, except for domain-mean supersaturation with respect to liquid water, S_{liq}, as a function of mean cloud chamber temperature for all sensitivity experiments. The horizontal dashed line marks S_{liq} = 0, with negative values indicating liquid-water subsaturation and positive values indicating liquid-water supersaturation.

https://doi.org/10.5194/egusphere-2026-6098
Preprint. Discussion started: 12 November 2026
© Author(s) 2026. CC BY 4.0 License.

Figure 9 shows the corresponding domain-mean ice mixing ratio Q_{ice} for the same set of simulations. The top row displays the polluted Seoul cases and the bottom row the clean cases, while the left and right columns separate the EVAP and NOEVAP simulations. For a given aerosol loading, slower ascent rate generally leads to smaller Q_{ice} throughout the mixed-phase layer. This behavior reflects the stronger cumulative impact of sedimentation loss at lower ascent rates. Since the imposed ascent rate sets the cooling rate in the chamber, a slower ascent rate requires a longer physical time to reach a comparable thermodynamic state, thereby allowing greater hydrometeor loss from the finite 2 m chamber.

Comparison of the polluted and clean cases at the same ascent rate indicates that Q_{ice} is systematically smaller in the clean cases (Fig. 9). With a lower soluble aerosol concentration, fewer but larger droplets are produced, reducing the total liquid surface area and enhancing droplet sedimentation. This limits the liquid reservoir available for subsequent freezing and depositional growth, shifting the clean Q_{ice} curves downward relative to their polluted counterparts. For both aerosol regimes, the EVAP simulations generally produce larger Q_{ice} than the corresponding NOEVAP simulations, particularly at moderate and large ascent rates. This implies that droplet evaporation under liquid-subsaturated conditions provides an important additional vapor source for depositional growth of ice crystals. The corresponding liquid droplet and ice crystal number concentrations support this interpretation because of the lower droplet number concentrations and higher ice crystal number concentrations in EVAP than in NOEVAP (Figs. S3 and S4). At smaller ascent rates, Q_{ice} remains small and exhibits stronger variability with temperature. This behavior reflects two related effects. First, slower cooling produces weaker supersaturation production, as indicated by the smaller S_{liq} in Fig. 8, particularly in the polluted EVAP cases near −20 °C. Second, a weaker ascent requires a longer physical time to reach a given temperature, allowing sedimentation and wall losses to remove more hydrometeors from the finite chamber. As a result, the ice reservoir remains small and is sensitive to droplet freezing, depositional growth, sedimentation, and boundary-loss events. The super-droplet count-loss rates separated by removal pathway further show that side-wall and upper-boundary losses become more important after ice formation as turbulence increases (Fig. S1). Thus, liquid droplet evaporation, ascent rate, aerosol loading, supersaturation evolution, and chamber-scale hydrometeor loss all jointly control ice production and growth in the finite-depth expansion chamber.

https://doi.org/10.5194/egusphere-2026-6098
Preprint. Discussion started: 12 November 2026
© Author(s) 2026. CC BY 4.0 License.

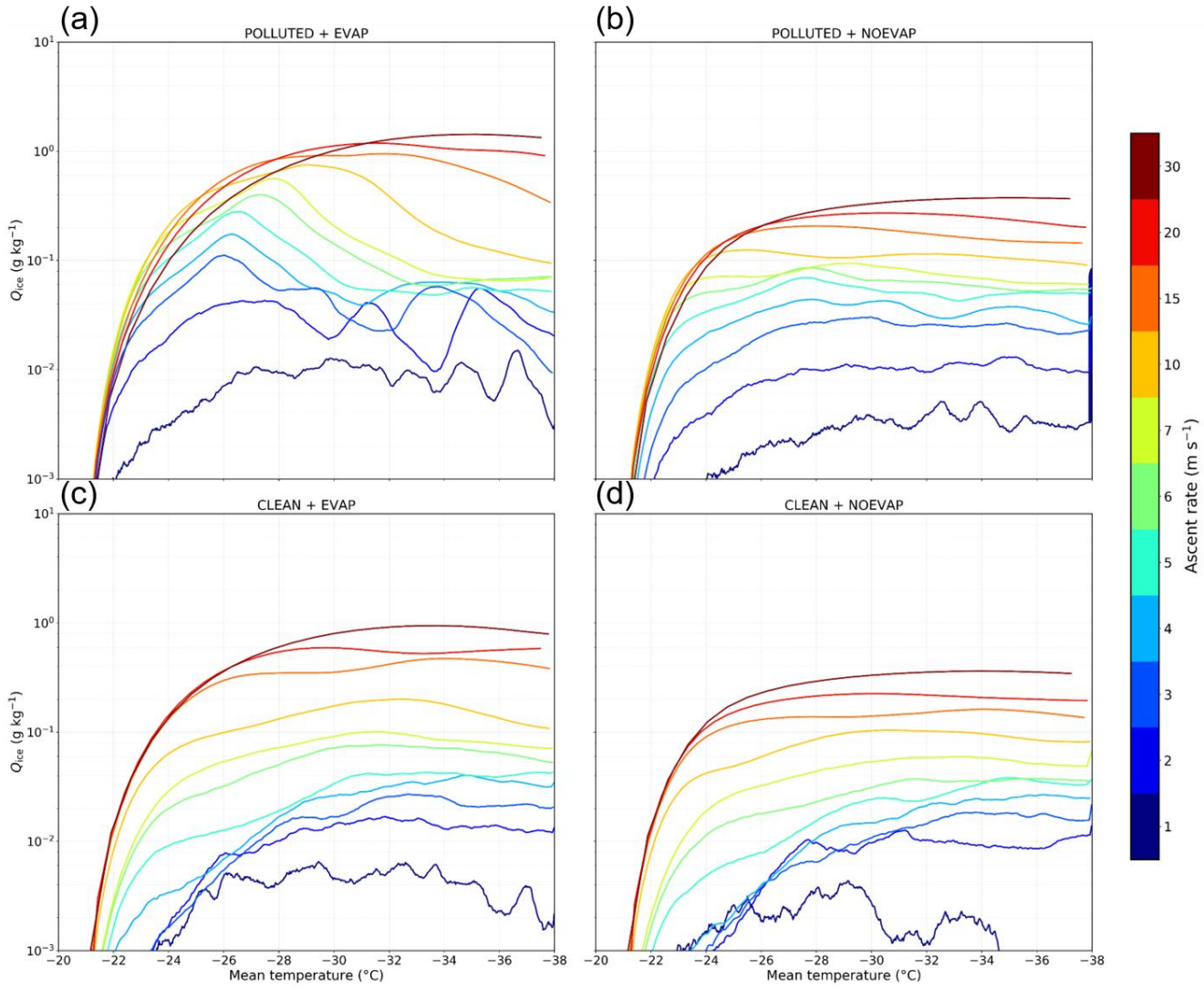


Figure 9. Same as Fig. 7, except for domain-mean ice mixing ratio Q_{ice} as a function of mean cloud chamber temperature for all sensitivity simulations.

Figure 10 shows the corresponding domain-mean ice mass fraction, defined as $f_{ice}=100\times Q_{ice}/(Q_{liq}+Q_{ice})$, for the same sensitivity simulations (Q_{liq} is the domain-averaged cloud water mixing ratio). In the NOEVAP simulations, f_{ice} remains far below 100% for all ascent rates, indicating that a persistent liquid reservoir is maintained when droplet evaporation is suppressed. In contrast, the EVAP simulations, especially in the polluted Seoul regime, often approach an ice-dominated state, with f_{ice} close to 100 %, over the mixed-phase temperature range. The temperature at which f_{ice} approaches 100% shows a nonmonotonic dependence on ascent rate. From w between 2 and 6 m s^{-1}, increasing w shifts the transition toward warmer temperatures, corresponding to an earlier time in the chamber simulation. In the chamber framework, a larger ascent rate

https://doi.org/10.5194/egusphere-2026-6098
Preprint. Discussion started: 12 November 2026
© Author(s) 2026. CC BY 4.0 License.

corresponds to a faster cooling rate, so a given temperature is reached at an earlier physical time. This reduces the time available for sedimentation loss and helps maintain a larger in-chamber liquid reservoir that can subsequently contribute to ice growth once WBF-favorable subsaturation develops. For w larger than 6 m s^{-1}, the tendency reverses: f_{ice} approaches 100% at colder temperatures because faster cooling shortens the physical time available for depositional ice growth within the mixed-phase temperature interval. Thus, even when WBF-favorable conditions are reached, ice crystals may not grow sufficiently before the chamber temperature decreases further. Such turnover highlights the competition between sedimentation-controlled water retention at low-to-moderate ascent rates and time-limited depositional growth at high ascent rates, and it helps explain why complete glaciation is most readily achieved in the polluted EVAP cases at intermediate ascent rates. In the clean regime, f_{ice} generally approaches unity only near the homogeneous-freezing limit (approximately −38 °C) because droplets are fewer and larger, sedimentation losses are stronger and the total liquid surface area (and thus evaporation-driven vapor supply) is reduced. All of these effects weaken WBF-mediated liquid-to-ice conversion compared with the polluted cases.

After examining the Q_{ice} and f_{ice} responses, we next assess whether their nonmonotonic dependence on the ascent rate can be explained simply by the time spent under WBF-favorable conditions. Table 1 summarizes residence-time diagnostics for some selected realistic simulations (i.e., with gravity and droplet evaporation included): time spent in −22 to −37 °C temperature range under WBF favorable ($S_{liq} < 0$ and $S_{ice} > 0$) conditions or under $u_z^* > 1$ conditions. The temperature warm boundary of -22 °C was chosen because the ice fraction begins to increase appreciably below this temperature, whereas the cold boundary of -37 °C excludes the rapid transition near the homogeneous-freezing threshold at approximately -38 °C (Fig. 10). The duration of the thermodynamic WBF-favorable condition mainly reflects the physical time spent in this temperature range. In the polluted cases, this duration increases strongly as the ascent rate decreases. However, the duration for which u_z^* exceeds unity does not show the same monotonic dependence, indicating that a longer residence time does not necessarily imply a persistently strong ice depositional vapor sink.

Table 1 also shows height intervals corresponding to WBF-favorable and $u_z^* > 1$ time durations (the third and fourth columns, respectively). These diagnostics highlight the impact of the ascent rate and CCN characteristics. For the polluted cases, the thermodynamic WBF-favorable height intervals are broadly similar over a wide range of ascent rates, whereas the corresponding $u_z^* > 1$ height interval is the largest at an intermediate ascent rate. In the clean cases, the smallest ascent rate case does not even enter the WBF-favorable thermodynamic condition within this temperature range, and the largest exposure also occurs at intermediate ascent rates. These results indicate that the simulated ice response is not controlled by residence time alone, but by the combined effects of supersaturation production, freezing, ice surface area, depositional growth, and hydrometeor loss. These sensitivity results are summarized below using a WBF index that combines the EVAP–NOEVAP response with the diagnosed vapor-sink strength. The key conclusion is that the microphysical processes within the simulated expansion cloud chamber involve complex interactions between macrophysical (i.e., the ascent rate, chamber depth) and microphysical (i.e., CCN characteristics, ice formation mechanisms) parameters.

https://doi.org/10.5194/egusphere-2026-6098
Preprint. Discussion started: 12 November 2026
© Author(s) 2026. CC BY 4.0 License.

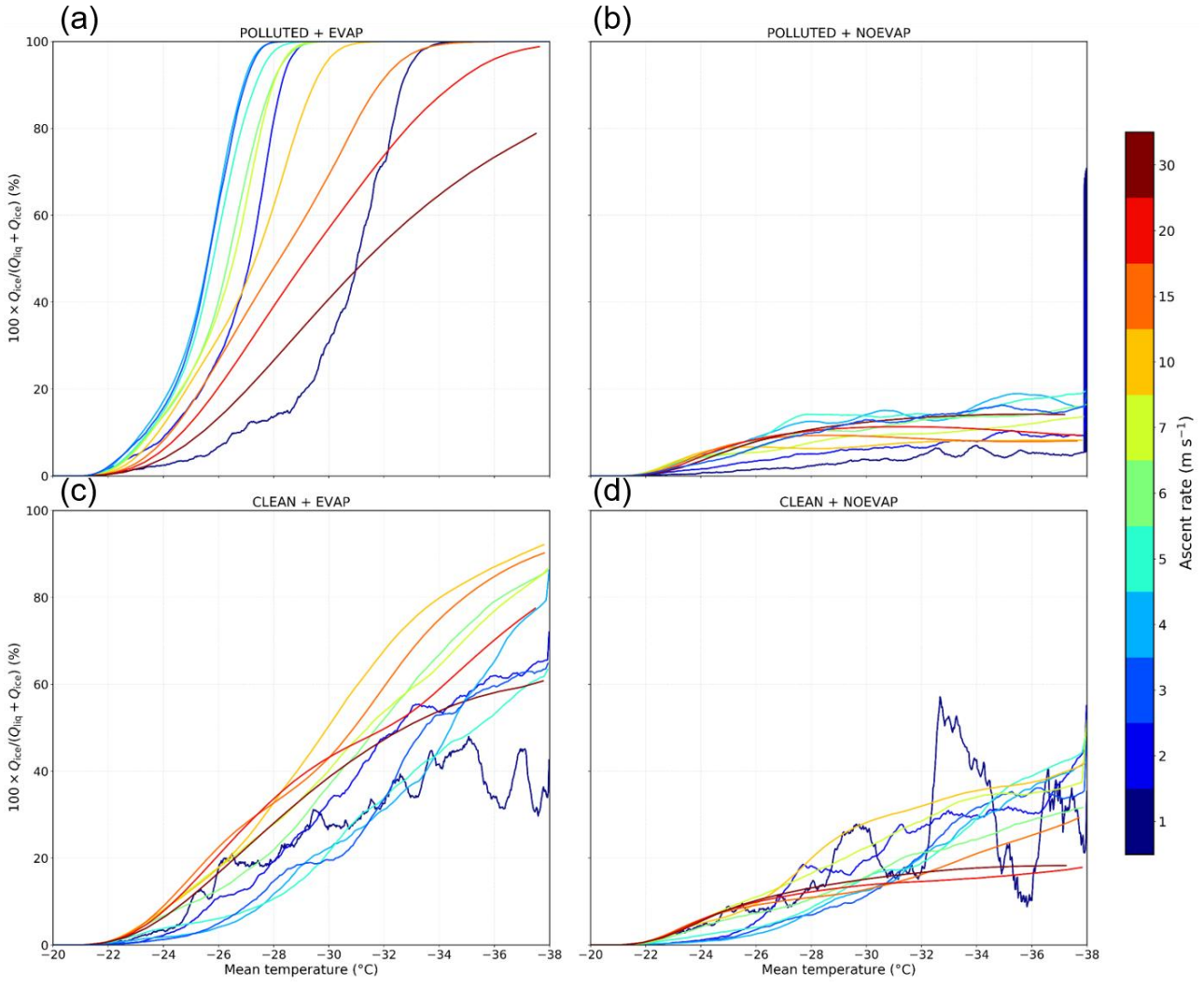


Figure 10. Same as Fig. 7, except for domain-mean ice mass fraction as a function of mean cloud chamber temperature for all sensitivity simulations.

https://doi.org/10.5194/egusphere-2026-6098
Preprint. Discussion started: 12 November 2026
© Author(s) 2026. CC BY 4.0 License.

Table 1. Residence-time diagnostics for selected realistic simulations within the −22 to −37 °C temperature range. The thermodynamic WBF-favorable condition is defined as $S_{liq} < 0$ and $S_{ice} > 0$. The condition $u_z^* > 1$ indicates that the diagnosed ice-depositional sink exceeds the supersaturation source produced by expansion cooling within the bulk approximation. The product $w\Delta t$ represents the equivalent interval in the ascent coordinate rather than the physical height of the 2 m chamber. Here, Δt denotes the duration of the corresponding condition.

Aerosol regime	w (m s^{-1})	WBF favorable duration (s)	Equivalent ascent interval during WBF-favorable duration (m)	Duration with $u_z^* > 1$ (s)	Equivalent ascent interval with $u_z^* > 1$ (m)
Polluted	1	1728	1728	156	156
Polluted	3	585	1755	234	702
Polluted	15	117	1755	111	1665
Polluted	30	54	1620	51	1530
Clean	1	0	0	0	0
Clean	3	198	594	78	234
Clean	15	75	1125	105	1575
Clean	30	33	990	51	1530

3.4 Dependence of WBF-driven ice growth on ascent rate, aerosol loading, and sedimentation loss

To summarize the sensitivity simulations, we combine the paired EVAP and NOEVAP simulations into two scalar diagnostics for each simulation. For each simulation, we compute $\overline{Q_{ice}^{EVAP}}$ and $\overline{Q_{ice}^{NOEVAP}}$ by averaging the domain-mean ice mixing ratio over the selected chamber-temperature range for EVAP and NOEVAP simulations. Using a cloud-ice mixing-ratio threshold of $Q_{ice} \geq 0.01$ g kg^{-1}, consistent with thresholds used to distinguish cloudy conditions in previous cloud-resolving studies (e.g., Li et al., 2020), we retain only output times for which both EVAP and NOEVAP satisfy this criterion. More importantly, we restrict the averaging temperature window to −22 to −37 °C to target temperatures where ice is consistently present. Ice content becomes appreciable below about −22 °C because of the INP activity formulation, while excluding the colder end near the homogeneous-freezing regime (around −38 °C) avoids the region where ice production can change abruptly and bias the averages, as shown in Fig. 10b. We then define the WBF index as

$$dQ_{ice} = 100 \times (\overline{Q_{ice}^{EVAP}} - \overline{Q_{ice}^{NOEVAP}}) / \overline{Q_{ice}^{NOEVAP}} \quad . \tag{5}$$

This index quantifies the relative enhancement of ice mass attributable to droplet evaporation and the associated WBF growth pathway.

https://doi.org/10.5194/egusphere-2026-6098
Preprint. Discussion started: 12 November 2026
© Author(s) 2026. CC BY 4.0 License.

For each paired EVAP and NOEVAP simulation, we also calculate the mean of the domain-average u_z^* from the EVAP simulation over the same temperature range and WBF-favorable durations. Figure 11 summarizes the paired EVAP–NOEVAP response for all ascent rates, aerosol regimes, and gravity configurations. The x-coordinate is given by the mean u_z^* from the EVAP simulation, and the y-coordinate shows the EVAP–NOEVAP difference in Q_{ice} (Fig. 11a) or $\Delta f_{ice}=f_{ice}^{EVAP}-f_{ice}^{NOEVAP}$, the enhancement in ice mass fraction due to evaporation (Fig. 11b). Each point represents one pair of simulations with the same ascent rate, aerosol loading, and gravity setting. Blue symbols denote simulations with gravity-on, and orange symbols denote no-gravity simulations, in which gravitational settling is disabled. Circles and triangles denote simulation pairs with polluted Seoul aerosol and with clean cases in which total aerosol concentrations were reduced by a factor of 10, respectively. Figure 11 a documents the critical impact of the particle sedimentation inside the chamber on the details of the WBF ice growth regime for the dQ_{ice}. Only at ascent rates above about 10 and 15 m s^{-1} for polluted and clean aerosol, respectively, do the gravity-on and no-gravity results occupy similar regions of the diagrams. In the polluted (Seoul) gravity-on simulations, dQ_{ice} generally increases with ascent rate up to about 15 m s^{-1}. This is consistent with stronger ascent rates partly offsetting sedimentation loss and allowing more condensate to remain in the chamber to participate in WBF-driven depositional growth. At higher ascent rates ($w > 15$ m s^{-1}), dQ_{ice} decreases despite u_z^* being much larger than unity, indicating a transition to a regime in which the limited residence time in the mixed-phase temperature range becomes the dominant constraint on depositional growth and WBF.

Figure 11b complements the above mass-based metric by showing the enhancement in ice mass fraction due to evaporation, expressed in percentage points. In the polluted gravity-on simulations, Δf_{ice} increases from w = 1 m s^{-1} to a maximum at w = 3 m s^{-1}, and then generally decreases at higher ascent rates. Thus, the evaporation-induced shift in phase partitioning is strongest at an intermediate ascent rate rather than increasing continuously with w.

In the clean cases, where the soluble aerosol concentration is reduced by a factor of ten, the relative ice-mass enhancement dQ_{ice} also remains smaller than in the polluted cases over most of the gravity-on simulations, with values generally below about 200%. Unlike the polluted cases, Δf_{ice} in the clean gravity-on simulations are small and shows an overall increasing tendency with ascent rate. The lower soluble aerosol concentration produces fewer and larger liquid droplets, which have larger fall speeds and are therefore more susceptible to sedimentation loss. At low ascent rates, sedimentation acts over a longer physical time and strongly suppresses the EVAP–NOEVAP response. As the ascent rate increases, the time available for sedimentation decreases, allowing more condensate to remain in the chamber.

In the high-ascent-rate regime, dQ_{ice} of the polluted gravity-on simulations becomes similar to that of the no-gravity simulations, consistent with the reduced importance of sedimentation when cooling is very rapid. The no-gravity simulations show a more monotonic behavior that reflects the residence-time effect directly. For both aerosol cases, dQ_{ice} decreases systematically as the ascent rate increases. The same tendency is also evident in the ice-fraction enhancement, Δf_{ice}: in the absence of sedimentation, Δf_{ice} is largest at the slowest ascent rates and declines as ascent rate becomes faster, indicating a progressively smaller evaporation-driven shift in phase partitioning under rapid cooling. A smaller ascent rate implies a longer time spent in the mixed-phase temperature range, so conditions favorable for depositional ice growth persist for a longer period

https://doi.org/10.5194/egusphere-2026-6098
Preprint. Discussion started: 12 November 2026
© Author(s) 2026. CC BY 4.0 License.

and ice crystals have more time to grow at the expense of liquid droplets. In other words, the slower-ascent-rate simulations in the no-gravity limit experience stronger WBF and therefore produce both larger relative ice-mass enhancement dQ_{ice} and a larger increase in ice mass fraction Δf_{ice} than the faster-ascent-rate simulations.

https://doi.org/10.5194/egusphere-2026-6098
Preprint. Discussion started: 12 November 2026
© Author(s) 2026. CC BY 4.0 License.

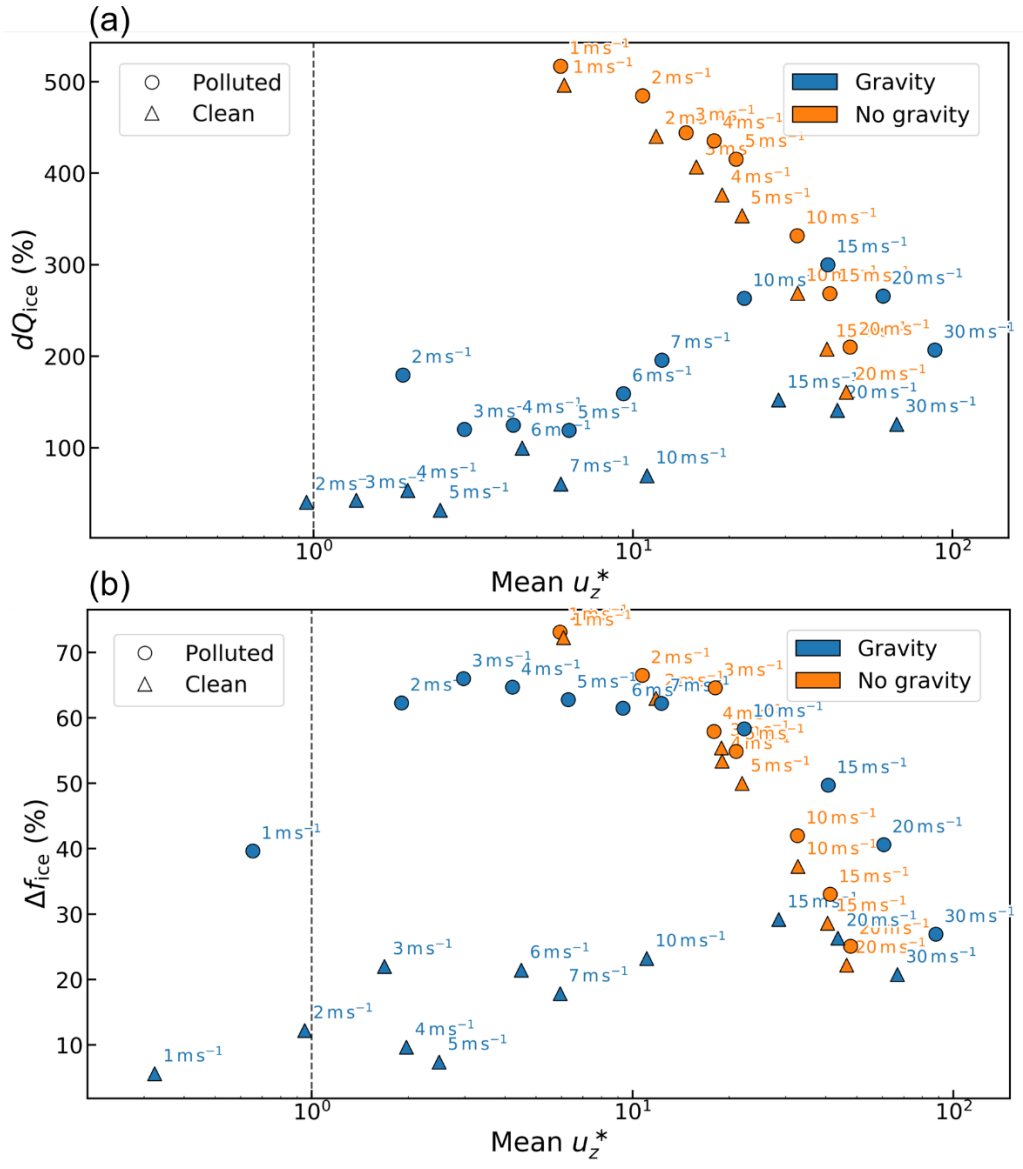


Figure 11. EVAP–NOEVAP response metrics as functions of the mean normalized effective ascent-rate diagnostic, u_z^*. In both panels, the x coordinate is the mean u_z^* from the EVAP simulation over the -37 to -22 °C temperature interval. Panel (a) shows the relative ice-mass enhancement, dQ_{ice}, calculated using only output times for which both Q_{ice}^{EVAP} and Q_{ice}^{NOEVAP} exceed 0.01 g kg^{-1}. Panel (b) shows the ice-fraction enhancement, $\Delta f_{ice}=f_{ice}^{EVAP}-f_{ice}^{NOEVAP}$, in percentage points, calculated over valid output times within the same temperature interval. Blue and orange symbols denote gravity-on and no-gravity simulations, respectively. Circles indicate the polluted Seoul aerosol cases, and triangles indicate the clean cases with N_{sol} reduced by a factor of 10. Point labels give the imposed ascent rate, and the vertical dashed line marks $u_z^* = 1$. Cases with no output times satisfying the common ice-content criterion are omitted from panel (a).

https://doi.org/10.5194/egusphere-2026-6098
Preprint. Discussion started: 12 November 2026
© Author(s) 2026. CC BY 4.0 License.

In summary, in the polluted Seoul regime, both dQ_{ice} and Δf_{ice} increase from low to intermediate ascent rates, indicating an active WBF regime in which liquid droplets are retained long enough to evaporate and supply vapor for ice growth. At higher ascent rates, both metrics decrease, even though u_z^* remains large, because rapid cooling shortens the time available for depositional growth. In contrast, the clean regime shows weaker WBF signatures because fewer, larger droplets sediment more efficiently and provide a smaller liquid surface area for evaporation. The no-gravity simulations further show that, when sedimentation is neglected, the response is controlled mainly by residence time and becomes more monotonic with the ascent rate. Thus, real chamber experiments may exhibit three regimes: sedimentation-limited growth at low ascent rates, efficient WBF-driven liquid-to-ice conversion at intermediate ascent rates, and time-limited depositional growth at high ascent rates.

To further connect these WBF response metrics to the thermodynamic saturation state, we diagnose in Fig. 12 the WBF saturation-state parameter $\chi_{WBF} = (e - e_{s,i})/(e_{s,w} - e_{s,i})$ for the EVAP simulations, averaged over the same −22 to −37 °C temperature range as done in Fig. 11. Values of $0 < \chi_{WBF} < 1$ indicate that vapor pressure is between saturation over ice and saturation over liquid water, corresponding to thermodynamic conditions favorable for WBF. Figure 12 shows that the polluted cases with gravity generally have lower mean χ_{WBF} than the clean cases, indicating a stronger and more persistent departure from liquid saturation. In contrast, the clean cases remain closer to liquid saturation, and in some cases mean χ_{WBF} exceeds unity, suggesting that WBF-favorable conditions are delayed to colder temperatures and are less persistent over the averaging interval. The ascent-rate dependence of χ_{WBF} also supports the turnover interpretation in Fig. 11. In detail, in the gravity-on simulations, mean χ_{WBF} decreases from low to intermediate ascent rates and then increases again at higher ascent rates, consistent with the competition between sedimentation loss at low ascent rates and time-limited depositional growth at high ascent rates. In the no-gravity simulations, mean χ_{WBF} increases monotonically with ascent rate, indicating that slower ascent allows a larger departure from liquid saturation, whereas faster ascent keeps the chamber closer to liquid saturation. There is little difference between polluted and clean aerosol simulations in no-gravity simulations. The full temperature-dependent evolution of χ_{WBF} is provided in the Figure S6.

https://doi.org/10.5194/egusphere-2026-6098
Preprint. Discussion started: 12 November 2026
© Author(s) 2026. CC BY 4.0 License.

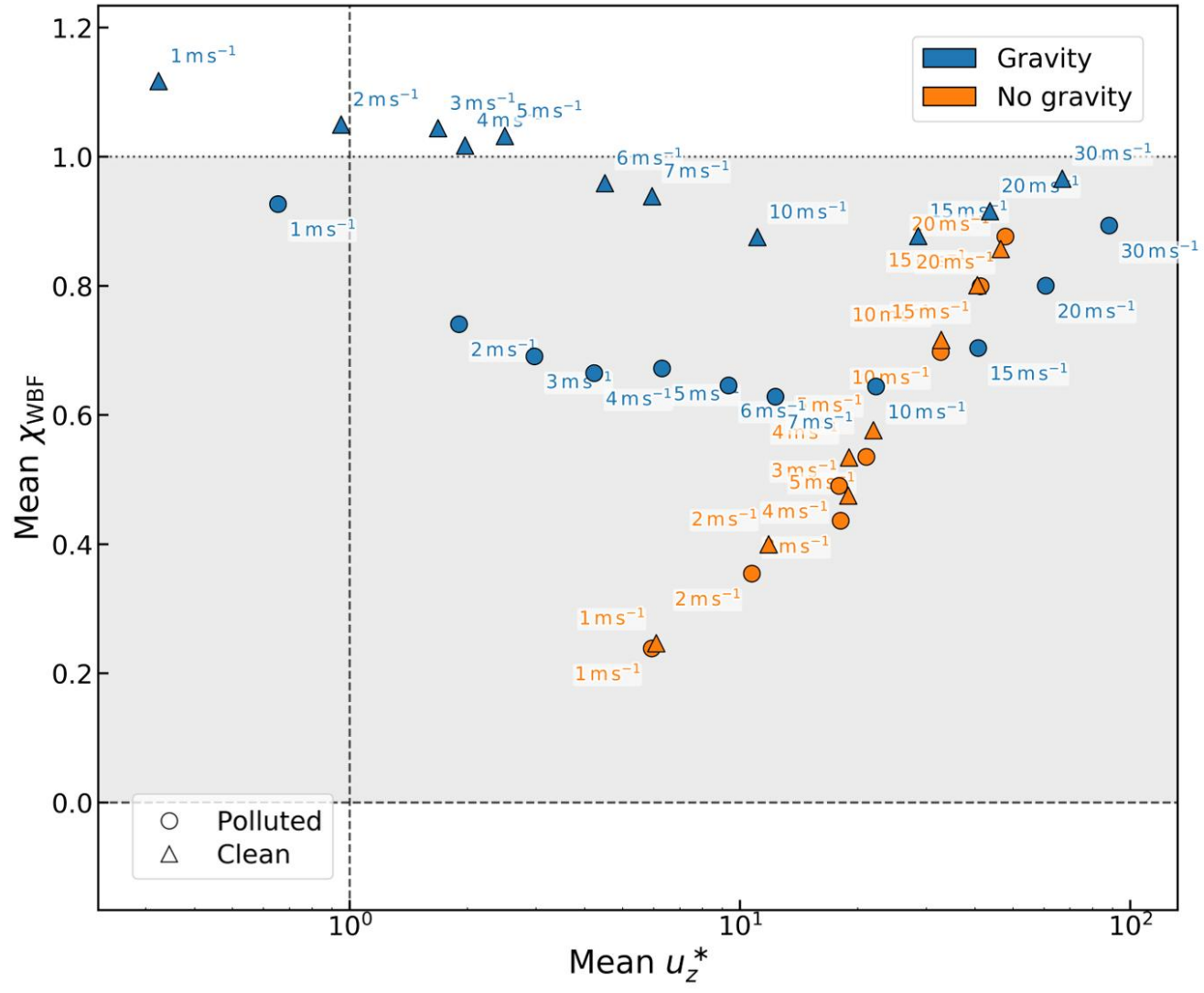


Figure 12. Mean thermodynamic WBF-regime parameter, χ_{WBF}, as a function of the mean normalized effective ascent-rate diagnostic, u_z^*, for the EVAP simulations. Both quantities are averaged over valid output times within the -37 to -22 °C temperature interval, consistent with the x-axis averaging used in Fig. 11. The shaded $0 < \chi_{WBF} < 1$ indicates vapor pressures between saturation over ice and saturation over liquid water and therefore thermodynamic conditions favorable for WBF. Blue and orange symbols denote gravity-on and no-gravity simulations, respectively. Circles indicate the polluted Seoul aerosol cases, and triangles indicate the clean cases with N_{sol} reduced by a factor of 10. Point labels give the imposed ascent rate.

https://doi.org/10.5194/egusphere-2026-6098
Preprint. Discussion started: 12 November 2026
© Author(s) 2026. CC BY 4.0 License.

3.5 Ice habit and apparent density: role of ascent rate and soluble aerosol

Following Shima et al. (2020), the present model implements condensation/immersion freezing and depositional ice growth processes. Detailed crystal habits are not explicitly resolved. Instead, ice particle morphology is characterized using the polar-to-equatorial radius ratio, r_p/r_e, and the apparent ice density. Here, r_p/r_e denote the polar and equatorial ice-particle radii, respectively. The ratio r_p/r_e evolves during depositional growth, for which the preferred growth direction is prescribed solely as a function of temperature through the inherent growth ratio $\Gamma(T)$. Values of $\Gamma(T)$ >1 favor polar growth and a more column-like tendency, whereas values of $\Gamma(T)$ < 1 favor equatorial growth and a more planar tendency (Chen and Lamb, 1994; Shima et al., 2020). Accordingly, r_p/r_e > 1 indicates a columnar geometry, whereas r_p/r_e < 1 indicates a planar geometry. Because the prescribed $\Gamma(T)$ exceeds unity below about −20 °C and is held constant at its −30 °C value at colder temperatures, the habit scheme favors polar growth over most of the cold mixed-phase range considered here.

Apparent ice density is diagnosed independently from the local depositional growth conditions and provides complementary information on particle structure. For columnar particles, low apparent density indicates hollow-column structures. For planar particles, high apparent density indicates plate-like ice, whereas low apparent density indicates dendritic or branched ice. However, the present habit prediction has substantial uncertainty at temperatures below −30 °C. In this temperature range, the inherent growth ratio is poorly constrained and is assumed to remain constant at its −30 °C value (Shima et al., 2020). Therefore, the simulated habit diagnostics below −30 °C should be interpreted with caution, as actual ice crystals may exhibit columnar, planar, or polycrystalline forms.

Figure 13 shows the mean r_p/r_e and apparent ice density as functions of mean temperature for the gravity-on simulations. In these gravity-on simulations, the differences between EVAP and NOEVAP are relatively small. This is likely because sedimentation modifies the particle population in the finite-depth chamber. At smaller ascent rates, the cooling is slower and particles remain longer in the mixed-phase temperature range, allowing larger, faster-falling ice particles to be removed more efficiently. In general, changes in mean r_p/r_e and apparent density should be interpreted as population effects caused by ice growth, sedimentation, and replenishment, not as density increase of individual ice particles. In the NOEVAP simulations, ice growth is weaker, so ice particles remain smaller on average and sediment less efficiently. This allows elevated r_p/r_e values to persist longer in some NOEVAP cases, especially at higher ascent rates. The clean case with w = 1 m s^{-1} should be interpreted cautiously because very little ice is present, making the r_p/r_e and density diagnostics noisy.

https://doi.org/10.5194/egusphere-2026-6098
Preprint. Discussion started: 12 November 2026
© Author(s) 2026. CC BY 4.0 License.

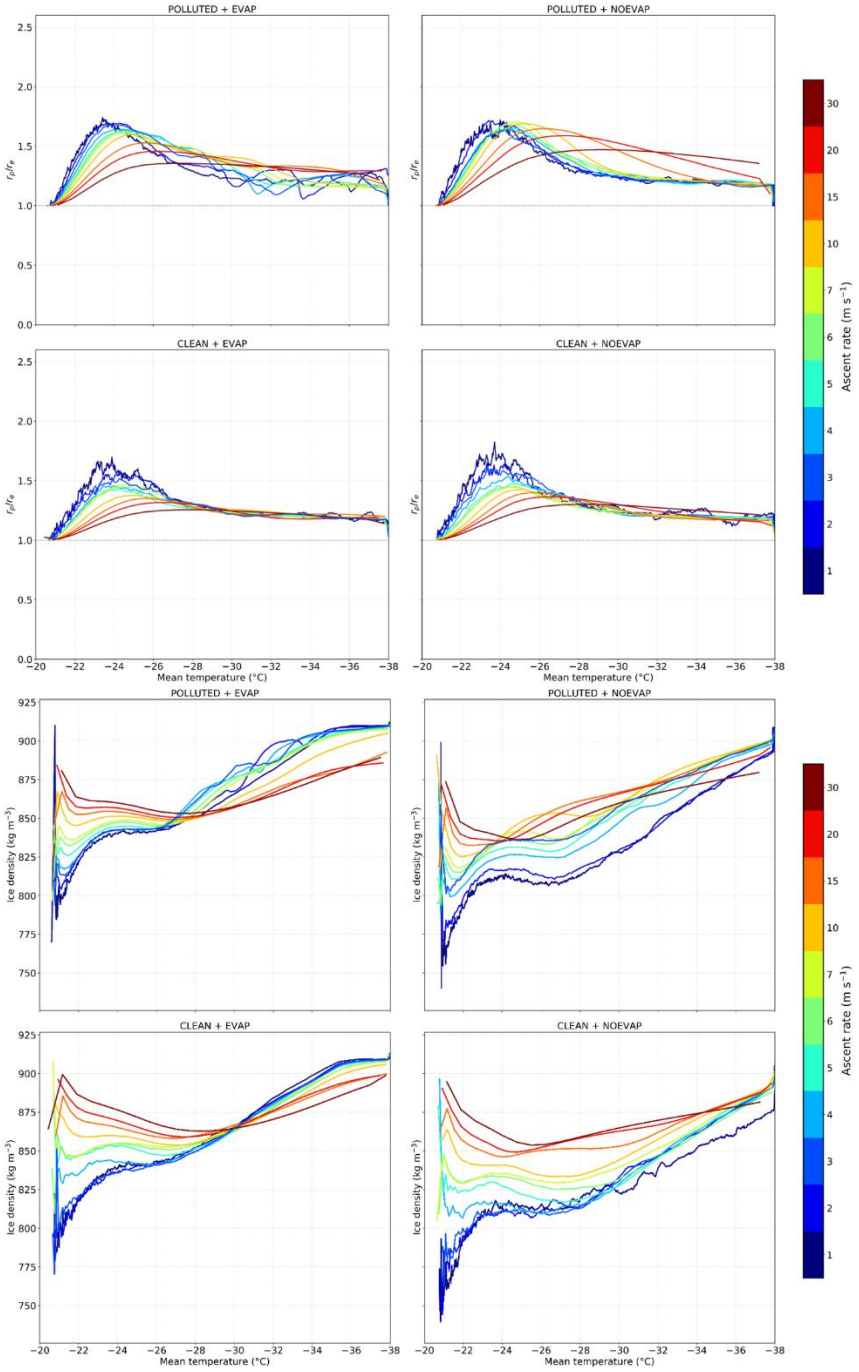


Figure 13. Mean polar (r_p) to equatorial radius (r_e) ratio r_p/r_e (top four panels) and mean apparent ice density (bottom four panels) as functions of mean temperature for simulations with gravity. Left and right columns show EVAP and NOEVAP simulations, and rows show the clean and polluted aerosol cases. Line color indicates the imposed ascent rate from 1 to 30 m s^{-1}.

https://doi.org/10.5194/egusphere-2026-6098
Preprint. Discussion started: 12 November 2026
© Author(s) 2026. CC BY 4.0 License.

Figure 14 shows the corresponding habit and apparent-density diagnostics for the no-gravity simulations. The EVAP–NOEVAP differences in ice habit become clearer because sedimentation no longer removes particles from the chamber. Under polluted EVAP conditions, slower ascents generally produce larger r_p/r_e and lower apparent density, indicating that longer mixed-phase residence time allows WBF-driven depositional growth to produce more nonspherical and lower-density ice particles. As the ascent rate increases, the peak r_p/r_e and the density reduction weaken, consistent with the shorter time available for depositional habit evolution.

However, the ascent-rate dependence of r_p/r_e is not strictly monotonic. In the reference no-gravity EVAP case, r_p/r_e reaches a maximum at an intermediate ascent rate, near 5 m s^{-1}. This behavior suggests competition between residence time and vapor depletion. Slower ascent increases the time available for depositional growth, but when ice growth becomes very efficient, the ice population rapidly depletes S_{ice}, limiting further habit evolution. This interpretation is supported by the reduced-INP experiments: decreasing N_{INP} weakens the total depositional vapor sink and shifts the r_p/r_e maximum toward slower ascent rates; at very low N_{INP}, the response becomes nearly monotonic, with the largest r_p/r_e at the slowest ascent rate (Fig. S9).

The clean and NOEVAP simulations show weaker habit signals. In the clean cases, fewer and larger droplets reduce the liquid surface area and the evaporation-driven vapor supply, leading to smaller changes in r_p/r_e and apparent density. In the NOEVAP cases, suppressing liquid evaporation further weakens depositional growth, so r_p/r_e remains closer to unity and apparent density remains closer to that of compact ice. Thus, the habit and density diagnostics consistently indicate that stronger WBF-driven deposition favors more nonspherical, lower-density ice, whereas limited residence time, weak vapor supply, or sedimentation reduces this signal. The vertical structure of these diagnostics is shown in Supplementary Figs. S10 and S11. In representative gravity-on EVAP simulations, u_z^* and r_p/r_e are enhanced mainly in the lower part of the chamber, especially in the polluted case, whereas apparent ice density shows weaker vertical variation.

https://doi.org/10.5194/egusphere-2026-6098
Preprint. Discussion started: 12 November 2026
© Author(s) 2026. CC BY 4.0 License.

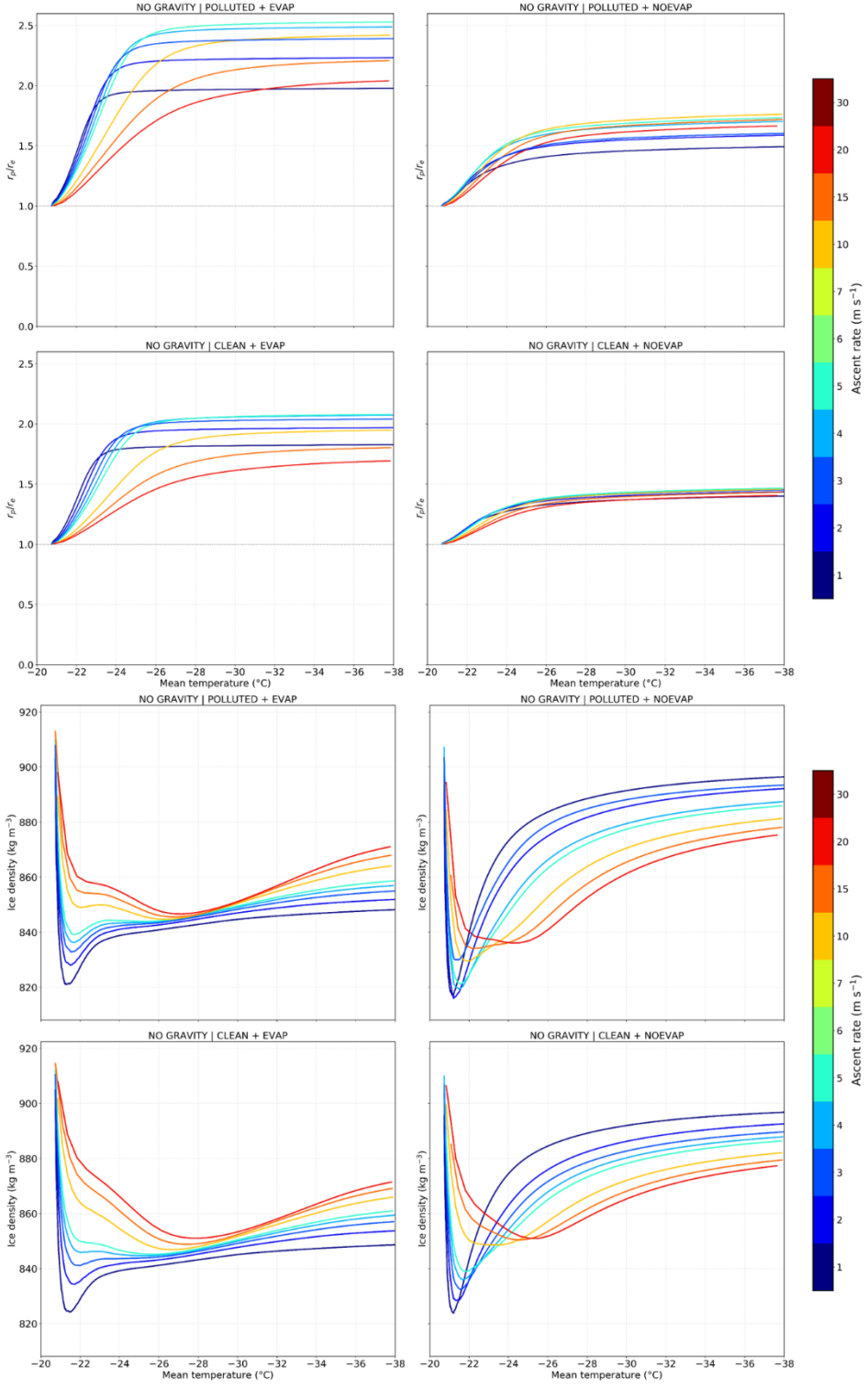


Figure 14. Same as in Figure 13, but for simulations without gravity.

https://doi.org/10.5194/egusphere-2026-6098
Preprint. Discussion started: 12 November 2026
© Author(s) 2026. CC BY 4.0 License.

4 Discussion

4.1 Implications for atmospheric mixed-phase clouds

Although the present chamber configuration is highly idealized, the results provide a useful framework for interpreting WBF activity in orographic mixed-phase clouds. In such clouds, the parcel ascent history controls both the cooling rate and the residence time within the mixed-phase temperature range. Previous Alpine case studies showed that changes in flow direction relative to the mountain range can modify the effective ascent history and thereby influence whether clouds remain mixed phase or glaciate more rapidly (Lohmann et al., 2016; Henneberg et al., 2017). In this context, the no-gravity chamber simulations provide an idealized limit that isolates the coupling among ascent history, ice surface area, vapor depletion, and WBF. The gravity-on simulations, in contrast, include the strong lower-boundary particle loss imposed by the 2-m-deep chamber. Real orographic clouds are expected to lie between these two limits: they are not sedimentation-free, but they are also not subject to the exaggerated hydrometeor removal associated with a finite-depth laboratory chamber.

Within this framework, gentle upslope flow corresponds to smaller effective ascent rates and longer residence times in the mixed-phase layer. The no-gravity simulations suggest that such conditions can enhance the integrated WBF response, as measured by dQ_{ice} and Δf_{ice}, once sufficient ice surface area has developed. In contrast, steeper and faster ascent may still produce $u_z^*>1$, indicating a strong instantaneous vapor sink by ice, but the shorter mixed-phase residence time limits the accumulation of depositional growth and allows supercooled liquid water to persist.

The habit diagnostics provide an additional link to atmospheric ice-particle geometry. In the no-gravity simulations, longer residence in the WBF temperature range promotes larger r_p/r_e and lower apparent density, indicating more nonspherical and lower-density ice particles. However, because $\Gamma(T)$ is assumed to remain constant below −30 °C owing to the lack of observational constraints, the habit interpretation in the colder part of the trajectory remains uncertain and should be regarded as a model-dependent tendency. At the same time, the ascent-rate dependence of r_p/r_e is not always monotonic. In the reference no-gravity EVAP case, r_p/r_e reaches a maximum near w = 5 m s^{-1}. The N_{INP}-sensitivity experiments show that this maximum shifts with ice surface area: in the reduced-N_{INP} case (500 cm^{-3}), r_p/r_e peaks near w = 3 m s^{-1}, whereas in the very-low-N_{INP} case (50 cm^{-3}), the response becomes nearly monotonic, with the largest r_p/r_e at w = 1 m s^{-1} and decreasing r_p/r_e with increasing ascent rate (Figs. S7–S9). This indicates that habit evolution reflects a balance between residence time and vapor depletion: slow ascent gives more time for growth, but a large ice population can rapidly reduce S_{ice} and terminate sustained habit evolution.

The apparent-density response can be interpreted using the Chen and Lamb (1994) deposition-density scheme as implemented by Shima et al. (2020). In this scheme, the vapor density difference $\Delta\rho_i$ determines the deposition density ρ_{dep}, defined as the density assigned to newly deposited ice mass during vapor growth. Large $\Delta\rho_i$ near −20 °C produces low ρ_{dep}, corresponding to porous growth that may be branched or hollowed depending on particle geometry, and causes the apparent ice density to decrease. As vapor is depleted, S_{ice} and $\Delta\rho_i$ decrease, ρ_{dep} approaches the solid-ice density, and the apparent density partly recovers. This explains the density minimum in Fig. 14 and its stronger sensitivity to ascent rate and soluble

https://doi.org/10.5194/egusphere-2026-6098
Preprint. Discussion started: 12 November 2026
© Author(s) 2026. CC BY 4.0 License.

aerosol concentration in the no-gravity simulations. With gravity, sedimentation weakens this habit-related signal by modifying the particle population in the finite chamber.

A qualitatively similar aerosol sensitivity of ice aspect ratio was reported by Lee et al. (2024), who used a $\Gamma(T)$-based habit-prediction framework in idealized stratiform mixed-phase clouds. They found that increasing soluble aerosol and INP concentrations reduced the aspect ratio and strengthened the dominance of oblate-like crystals between about −16 and −20 °C, consistent with $\Gamma(T) < 1$ in that temperature range. Together with the present chamber results, this suggests that aerosol-induced habit changes depend not only on the strength of WBF and the residence time in the mixed-phase regime, but also on the temperature range over which growth occurs. This is because $\Gamma(T)$ determines whether deposition favors column-like or plate-like growth. In the present chamber simulations, polluted cases with many small droplets develop stronger column-dominated habit signatures, characterized by larger r_p/r_e and lower apparent density, than clean cases with fewer, larger droplets. By analogy, aerosol loading in mountain environments may influence not only WBF strength, but also ice-particle aspect ratio in orographic mixed-phase clouds.

Taken together, the chamber simulations and orographic case studies suggest that u_z^*, mixed-phase residence time, sedimentation efficiency, aerosol loading, and the paired glaciation indices dQ_{ice} and Δf_{ice} provide a useful set of relevant variables for interpreting both laboratory simulations and atmospheric mixed-phase clouds.

4.2 Limitations and outlook

The idealizations employed in this study limit the direct application of the results to real clouds. First, the expansion forcing is spatially uniform and prescribed in time, so temperature and pressure decrease at the same rate throughout the chamber. Second, the boundary conditions are idealized: the mean chamber state is imposed at the walls, and the lower boundary acts as a perfect sink for sedimenting particles. These assumptions simplify the interpretation of sedimentation effects but may exaggerate the contrast between simulations with and without gravity relative to the real chamber, where wall roughness, secondary circulations, and possible particle recirculation may occur.

The aerosol and INP conditions are also simplified. The soluble aerosol population is represented by a single polluted Seoul distribution, and the dust INP population follows a prescribed size spectrum. In addition, the total N_{INP} is artificially increased to about 1,500 cm^{-3} in the main simulations to obtain clear WBF signals. Different aerosol and INP concentrations, size distributions, and mixing states could alter the magnitude and ascent-rate dependence of dQ_{ice}, Δf_{ice}, and the associated thermodynamic and habit responses. The present results should therefore be regarded as a qualitative assessment of how ascent rate, aerosol loading, and sedimentation interact in a finite chamber rather than as a universal quantitative WBF regime diagram. Sensitivity simulations with N_{INP} reduced to 50 cm^{-3} show that the detailed responses change with ice number concentration, while the broader roles of mixed-phase residence time and WBF activity remain robust (Figs. S7–S9).

The representation of ice morphology introduces an additional limitation. Ice morphology is diagnosed using the polar-to-equatorial radius ratio, r_p/r_e, and the apparent ice density following the parameterizations implemented by Shima et al. (2020). The prescribed growth-ratio relation $\Gamma(T)$ favors polar growth below about −20 °C and is held constant below

https://doi.org/10.5194/egusphere-2026-6098
Preprint. Discussion started: 12 November 2026
© Author(s) 2026. CC BY 4.0 License.

−30 °C because of limited observational constraints. Thus, r_p/r_e should be interpreted as a parameterization-dependent tendency rather than as a deterministic prediction of atmospheric crystal shape. Similarly, the apparent-density diagnostic depends on the Chen and Lamb (1994) deposition-density scheme, while processes not represented here, including riming, aggregation, secondary ice production, and mechanical breakup, could substantially modify particle morphology and density in natural mixed-phase clouds. Laboratory and field observations also indicate that ice habit depends on supersaturation and growth conditions in addition to temperature (Bailey and Hallett, 2004, 2009). The simulated habit and density responses should therefore be interpreted qualitatively when extrapolating them to atmospheric clouds.

Future work should extend this framework by sampling broader soluble aerosol and INP spectra, implementing more realistic chamber geometries and wall processes, and testing more flexible or probabilistic habit representations. Combining such chamber simulations with targeted observations and LES of orographic mixed-phase clouds under realistic topography and aerosol conditions will be needed to determine how aerosol and INP variability modulate WBF-driven habit evolution in the atmosphere and whether chamber-based constraints can inform improved parameterizations for weather and climate models.

5 Summary and conclusions

This study used a Lagrangian super-droplet model of a 2 m-high expansion cloud chamber to examine the conditions for favorable ice particle growth by the Wegener–Bergeron–Findeisen process (WBF) under the constraint of a finite-depth cloud chamber configuration. The model couples the babyEULAG dynamical core with condensation/immersion-freezing and depositional ice-growth schemes following Shima et al. (2020), and allows controlled variations of the ascent rate, aerosol loading, and sedimentation. The WBF response was quantified by estimating the two indices: dQ_{ice}, the evaporation-driven enhancement of ice mass, and Δf_{ice}, the corresponding increase in ice mass fraction, from the paired EVAP and NOEVAP simulations.

The main conclusion is that WBF signatures in a finite-depth cloud chamber are not controlled by vapor-sink strength alone, which was represented by u_z^*. Instead, they emerge from a competition between depositional growth time and hydrometeor loss. In the gravity-on polluted case simulations, WBF is the strongest at intermediate ascent rates. At low ascent rates, sedimentation removes droplets and ice particles before efficient liquid-to-ice conversion can develop, whereas at high ascent rates, rapid cooling limits the time available for depositional ice growth. This produces a turnover in dQ_{ice} and Δf_{ice} with the ascent rate. The no-gravity simulations confirm this interpretation by showing a more monotonic residence-time control when sedimentation is neglected.

Furthermore, aerosol loading modifies this balance by controlling the liquid reservoir available for evaporation. Polluted conditions produce more numerous, smaller droplets that are retained longer in the chamber and provide a larger surface area for evaporation over a longer period, leading to stronger WBF signatures. In contrast, the clean cases produce fewer, larger droplets that sediment more rapidly, reducing both the liquid reservoir and the evaporation-driven vapor supply.

https://doi.org/10.5194/egusphere-2026-6098
Preprint. Discussion started: 12 November 2026
© Author(s) 2026. CC BY 4.0 License.

Thus, even when u_z^* approaches or exceeds unity, a strong WBF response does not necessarily occur if liquid water is not sufficiently retained in the chamber.

The habit and apparent-density diagnostics support the same interpretation. In the absence of sedimentation, longer mixed-phase residence time allows stronger depositional habit evolution, whereas faster ascent tends to limit this evolution. With gravity-on, however, sedimentation alters the particle population and weakens the apparent separation between EVAP and NOEVAP and between aerosol regimes. These results show that chamber-scale particle loss can mask part of the microphysical signal.

Overall, finite chamber depth and gravitational settling place important constraints on the interpretation of chamber-based WBF experiments. The paired indices dQ_{ice} and Δf_{ice}, together with u_z^*, provide a useful framework for separating vapor-sink strength, liquid retention, and residence-time effects. A key implication is that WBF efficiency diagnosed in finite-depth chambers may underestimate the efficiency that would occur in deeper atmospheric mixed-phase clouds where hydrometeor loss by sedimentation would be weaker due to inherent updraft. Future work should test these conclusions under more realistic cooling histories, ice-nucleating particle spectra, and chamber geometries, and through comparison with in situ observations of orographic mixed-phase clouds.

Data availability The presented data are available from the corresponding author upon request (inyeob.la@gsis.u-hyogo.ac.jp).

Author contributions IL: Conceptualization, Methodology, Software, Formal analysis, Visualization, Writing – original draft. WWG: Conceptualization, Methodology, Writing – review and editing. SS: Methodology, Software, Writing – review and editing. SSY: Supervision, Funding acquisition, Writing – review and editing.

Competing interests The authors declare that they have no conflict of interest.

Acknowledgments. This work was supported by the KIST Institutional Grant (2E33101), the Yonsei Signature Research Cluster Program of 2024 (2024-22-0162), JSPS KAKENHI Grant Number 23H00149, and JST Moonshot R&D Grant Number JPMJMS2283.

References

Bailey, M. P. and Hallett, J.: Growth rates and habits of ice crystals between −20° and −70 °C, J. Atmos. Sci., 61, 514–544, https://doi.org/10.1175/1520-0469(2004)061<0514:GRAHOI>2.0.CO;2, 2004.

Bailey, M. P. and Hallett, J.: A comprehensive habit diagram for atmospheric ice crystals: Confirmation from the laboratory, AIRS II, and other field studies, J. Atmos. Sci., 66, 2888–2899, https://doi.org/10.1175/2009JAS2883.1, 2009.

Bergeron, T.: On the physics of clouds and precipitation, in: Proc. 5th Assembly of the International Union of Geodesy and Geophysics, Lisbon, Portugal, 1935, 156–180, 1935.

https://doi.org/10.5194/egusphere-2026-6098
Preprint. Discussion started: 12 November 2026
© Author(s) 2026. CC BY 4.0 License.

Chen, J. P. and Lamb, D.: The theoretical basis for the parameterization of ice crystal habits: Growth by vapor deposition, J. Atmos. Sci., 51, 1206–1222, https://doi.org/10.1175/1520-0469(1994)051<1206:TTBFTP>2.0.CO;2, 1994.

Connolly, P. J., Möhler, O., Field, P. R., Saathoff, H., Burgess, R., Choularton, T., and Gallagher, M.: Studies of heterogeneous freezing by three different desert dust samples, Atmos. Chem. Phys., 9, 2805–2824, https://doi.org/10.5194/acp-9-2805-2009, 2009.

Fan, J., Ghan, S., Ovchinnikov, M., Liu, X., Rasch, P. J., and Korolev, A.: Representation of Arctic mixed-phase clouds and the Wegener–Bergeron–Findeisen process in climate models: Perspectives from a cloud-resolving study, J. Geophys. Res., 116, D00T07, https://doi.org/10.1029/2010JD015375, 2011.

Findeisen, W.: Die kolloid-meteorologischen Vorgänge bei der Niederschlagsbildung, Meteorol. Z., 55, 121–133, 1938.

Grabowski, W. W.: Comparison of Eulerian bin and Lagrangian particle-based schemes in simulations of PI chamber dynamics and microphysics, J. Atmos. Sci., 77, 1151–1165, https://doi.org/10.1175/JAS-D-19-0216.1, 2020.

Grabowski, W. W., Morrison, H., Shima, S. I., Abade, G. C., Dziekan, P., and Pawlowska, H.: Modeling of cloud microphysics: Can we do better?, Bull. Am. Meteorol. Soc., 100, 655–672, https://doi.org/10.1175/BAMS-D-18-0005.1, 2019.

Grabowski, W. W., Kim, Y., and Yum, S. S.: CCN activation and droplet growth in Pi chamber simulations with Lagrangian particle-based microphysics, J. Atmos. Sci., 81, 1201–1212, https://doi.org/10.1175/JAS-D-24-0004.1, 2024.

Henneberg, O., Henneberger, J., and Lohmann, U.: Formation and development of orographic mixed-phase clouds, J. Atmos. Sci., 74, 3703–3724, https://doi.org/10.1175/JAS-D-16-0348.1, 2017.

Korolev, A.: Limitations of the Wegener–Bergeron–Findeisen mechanism in the evolution of mixed-phase clouds, J. Atmos. Sci., 64, 3372–3375, https://doi.org/10.1175/JAS4035.1, 2007.

Korolev, A. and Field, P. R.: The effect of dynamics on mixed-phase clouds: Theoretical considerations, J. Atmos. Sci., 65, 66–86, https://doi.org/10.1175/2007JAS2355.1, 2008.

Korolev, A. and Mazin, I. P.: Supersaturation of water vapor in clouds, J. Atmos. Sci., 60, 2957–2974, https://doi.org/10.1175/1520-0469(2003)060<2957:SOWVIC>2.0.CO;2, 2003.

Korolev, A. V., Isaac, G. A., Cober, S. G., Strapp, J. W., and Hallett, J.: Microphysical characterization of mixed-phase clouds, Q. J. R. Meteorol. Soc., 129, 39–65, https://doi.org/10.1256/qj.01.204, 2003.

Korolev, A., McFarquhar, G., Field, P. R., Franklin, C., Lawson, P., Wang, Z., Williams, E., Abel, S. J., Axisa, D., Borrmann, S., Crosier, J., Fugal, J., Krämer, M., Lohmann, U., Schlenczek, O., Schnaiter, M., and Wendisch, M.: Mixed-phase clouds: Progress and challenges, Meteorol. Monogr., 58, 5.1–5.50, https://doi.org/10.1175/AMSMONOGRAPHS-D-17-0001.1, 2017.

Kumar, P., Sokolik, I. N., and Nenes, A.: Parameterization of cloud droplet formation for global and regional models: including adsorption activation from insoluble CCN, *Atmos. Chem. Phys.*, **9**, 2517–2532, https://doi.org/10.5194/acp-9-2517-2009, 2009.

Kumar, P., Sokolik, I. N., and Nenes, A.: Measurements of cloud condensation nuclei activity and droplet activation kinetics of fresh unprocessed regional dust samples and minerals, *Atmos. Chem. Phys.*, **11**, 3527–3541, https://doi.org/10.5194/acp-11-3527-2011, 2011.

https://doi.org/10.5194/egusphere-2026-6098
Preprint. Discussion started: 12 November 2026
© Author(s) 2026. CC BY 4.0 License.

La, I., Grabowski, W. W., Kim, Y., Kim, S., and Yum, S. S.: Lagrangian particle–based simulation of aerosol-dependent vertical variation of cloud microphysics in a laboratory convection cloud chamber, Atmos. Chem. Phys., 26, 5213–5235, https://doi.org/10.5194/acp-26-5213-2026, 2026.

Lee, J., Seifert, P., Hashino, T., Maahn, M., Senf, F., and Knoth, O.: Simulations of the impact of cloud condensation nuclei and ice-nucleating particle perturbations on the microphysics and radar reflectivity factor of stratiform mixed-phase clouds, Atmos. Chem. Phys., 24, 5737–5756, https://doi.org/10.5194/acp-24-5737-2024, 2024.

Li, X., Krueger, S. K., Strong, C., Mace, G. G., and Benson, S.: Midwinter Arctic leads form and dissipate low clouds, *Nature Communications*, 11, 206, https://doi.org/10.1038/s41467-019-14074-5, 2020.

Lohmann, U. and Hoose, C.: Sensitivity studies of different aerosol indirect effects in mixed-phase clouds, Atmos. Chem. Phys., 9, 8917–8934, https://doi.org/10.5194/acp-9-8917-2009, 2009.

Lohmann, U., Henneberger, J., Henneberg, O., Fugal, J. P., Bühl, J., and Kanji, Z. A.: Persistence of orographic mixed-phase clouds, Geophys. Res. Lett., 43, 10512–10519, https://doi.org/10.1002/2016GL071036, 2016.

McCoy, D. T., Hartmann, D. L., Zelinka, M. D., Ceppi, P., and Grosvenor, D. P.: Mixed-phase cloud physics and Southern Ocean cloud feedback in climate models, J. Geophys. Res.-Atmos., 120, 9539–9554, https://doi.org/10.1002/2015JD023603, 2015.

Möhler, O., Field, P. R., Connolly, P., Benz, S., Saathoff, H., Schnaiter, M., Wagner, R., Cotton, R., Krämer, M., Mangold, A., and Heymsfield, A. J.: Efficiency of the deposition mode ice nucleation on mineral dust particles, Atmos. Chem. Phys., 6, 3007–3021, https://doi.org/10.5194/acp-6-3007-2006, 2006.

Morrison, H., de Boer, G., Feingold, G., Harrington, J., Shupe, M. D., and Sulia, K.: Resilience of persistent Arctic mixed-phase clouds, Nat. Geosci., 5, 11–17, https://doi.org/10.1038/ngeo1332, 2012.

Omanovic, N., Ferrachat, S., Fuchs, C., Henneberger, J., Miller, A. J., Ohneiser, K., Ramelli, F., Seifert, P., Spirig, R., Zhang, H., and Lohmann, U.: Evaluating the Wegener–Bergeron–Findeisen process in ICON in large-eddy mode with in situ observations from the CLOUDLAB project, Atmos. Chem. Phys., 24, 6825–6844, https://doi.org/10.5194/acp-24-6825-2024, 2024.

Park, M., Yum, S. S., Seo, P., Ahn, C., Kim, N., Anderson, B. E., and Thornhill, K. L.: A new CCN number concentration prediction method based on multiple linear regression and non-negative matrix factorization: 2. Application to obtain CCN spectra in and around the Korean Peninsula, J. Geophys. Res.-Atmos., 128, e2023JD039234, https://doi.org/10.1029/2023JD039234, 2023a.

Park, M., Yum, S. S., Seo, P., Kim, N., and Ahn, C.: A new CCN number concentration prediction method based on multiple linear regression and non-negative matrix factorization: 1. Development, validation, and comparison using the measurement data over the Korean Peninsula, J. Geophys. Res.-Atmos., 128, e2023JD039189, https://doi.org/10.1029/2023JD039189, 2023b.

https://doi.org/10.5194/egusphere-2026-6098
Preprint. Discussion started: 12 November 2026
© Author(s) 2026. CC BY 4.0 License.

Park, M., Cha, J. W., Park, S., Kim, J., Kim, Y., Belorid, M., Kim, B.-Y., Baek, J., Kim, S., Lee, K., Seo, P., Ahn, C., Lee, J., Yum, S. S., and Um, J.: Introduction to the Korea Cloud Physics Experimental Chamber (K-CPEC), Bull. Am. Meteorol. Soc., 106, E1897–E1918, https://doi.org/10.1175/BAMS-D-24-0330.1, 2025.

Pinsky, M. B., Khain, A. P., and Korolev, A.: Phase transformations in an ascending adiabatic mixed-phase cloud volume, J. Geophys. Res.-Atmos., 120, 3329–3353, https://doi.org/10.1002/2015JD023094, 2015.

Shima, S.-I., Kusano, K., Kawano, A., Sugiyama, T., and Kawahara, S.: The super-droplet method for the numerical simulation of clouds and precipitation: A particle-based and probabilistic microphysics model coupled with a non-hydrostatic model, Q. J. R. Meteorol. Soc., 135, 1307–1320, 2009.

Shima, S.-I., Sato, Y., Hashimoto, A., and Misumi, R.: Predicting the morphology of ice particles in deep convection using the super-droplet method: development and evaluation of SCALE-SDM 0.2.5-2.2.0, -2.2.1, and -2.2.2, Geosci. Model Dev., 13, 4107–4157, https://doi.org/10.5194/gmd-13-4107-2020, 2020.

Storelvmo, T., Kristjánsson, J. E., Lohmann, U., Iversen, T., Kirkevåg, A., and Seland, Ø.: Modeling of the Wegener–Bergeron–Findeisen process – implications for aerosol indirect effects, Environ. Res. Lett., 3, 045001, https://doi.org/10.1088/1748-9326/3/4/045001, 2008.

Storelvmo, T., Hoose, C., and Eriksson, P.: Global modeling of mixed-phase clouds: The albedo and lifetime effects of aerosols, J. Geophys. Res., 116, D05207, https://doi.org/10.1029/2010JD014724, 2011.

Tajiri, T., Yamashita, K., Murakami, M., Saito, A., Kusunoki, K., Orikasa, N., and Lilie, L.: A novel adiabatic-expansion-type cloud simulation chamber, J. Meteorol. Soc. Jpn. II, 91, 687–704, https://doi.org/10.2151/jmsj.2013-509, 2013.

Wang, A., Chen, S., Krueger, S. K., Dziekan, P., Enokido, K., Hoffmann, F., Makulska, A., Mehlig, B., Sardina, G., Sarnitsky, G., Schmalfuß, S., Shima, S.-i., Yang, F., Ovchinnikov, M., and Shaw, R. A.: A model intercomparison study of mixed-phase clouds in a laboratory chamber, J. Adv. Model. Earth Syst., 18, e2025MS005648, https://doi.org/10.1029/2025MS005648, 2026.

Wegener, A.: Thermodynamik der Atmosphäre, Johann Ambrosius Barth, Leipzig, 331 pp., 1911.

Yang, F., Sadi, H. F., Shaw, R. A., Hoffmann, F., Hou, P., Wang, A., and Ovchinnikov, M.: Microphysics regimes due to haze–cloud interactions: Cloud oscillation and cloud collapse, Atmos. Chem. Phys., 25, 3785–3806, https://doi.org/10.5194/acp-25-3785-2025, 2025.